Atlantic Hurricane response to Sahara greening and reduced dust emissions during the mid-Holocene

Samuel Dandoy[1], Francesco S.R. Pausata[1], Suzana J. Camargo[2], René Laprise[1], Katja Winger[1], and Kerry Emanuel[3]

[1]Department of Earth and Atmospheric Sciences, Université du Québec à Montréal
[2]Lamont-Doherty Earth Observatory, Columbia University, Palisades, NY, USA
Massachusetts Institute of Technology, Cambridge, MA,
[3]Program in Atmospheres, Oceans, and Climate, Massachusetts Institute of Technology, Cambridge, Massachusetts, USA

Correspondence to: Samuel Dandoy (dandoii@hotmail.ca)

Abstract. We use a high-resolution regional climate model to investigate the changes in Atlantic tropical cyclone (TC) activity during a period, the mid-Holocene (MH: 6,000 yrs BP) with a larger amplitude of the seasonal cycle relative to today. This period was characterized by increased boreal summer insolation over the Northern Hemisphere, a vegetated Sahara, and reduced airborne dust concentrations. A set of sensitivity experiments were conducted in which solar insolation, vegetation and dust concentrations were changed in turn to disentangle their impacts on TC activity in the Atlantic Ocean. Results show that the greening of the Sahara and reduced dust loadings (MH_{GS+RD}) lead to a larger increase in the number of Atlantic TCs (27%) relative to the pre-industrial climate (PI) than the orbital forcing alone (MH_{PMIP}; 9%). The TC seasonality is also highly modified in the MH climate, showing a decrease in TC activity during the beginning of the hurricane season (June to August), with a shift of its maximum towards October and November in the MH_{GS+RD} experiment relative to PI. MH experiments simulate stronger hurricanes compared to PI, similar to future projections. Moreover, they suggest longer lasting cyclones relative to PI. Our results also show that changes in the African Easterly Waves are not relevant in altering the frequency and intensity of TCs, but they may shift the location of their genesis. This work highlights the importance of considering vegetation and dust changes over the Sahara region when investigating TC activity under a different climate state.

1 Introduction

Tropical Cyclones (TCs) are one of the most powerful atmospheric phenomena on Earth. With increasing damages and costs due to natural disasters and recent upswing in Atlantic TCs, it becomes more and more important to understand how TC activity may change in the future. As TC development is strongly influence by, among others, vertical wind shear, sea surface temperature (SST) and humidity, changes in these environmental parameters due to climate change may result into large variability in TC activity. The on-going global warming can affect those environmental variables both directly by increasing the SST and indirectly through changes in the atmospheric stability and circulation. A recent study (Evan et al.,

2016) has shown that changes in atmospheric circulation at the end of the century could potentially reduce dust loadings over the tropical north Atlantic of around 10%. Evan et al. (2006) showed that Sahara dust layer is strongly linked to changes in North Atlantic TC activity, acting as an inhibiting factor for TC formation, as also previously suggested by Dunion & Velden (2004). These studies suggest that reducing the Sahara dust layer could lead to an increase in TC genesis occurrence, as well as more intense TCs by changes in the midlevel jet, directly impacting the vertical wind shear, and by increasing incoming solar radiation at the surface, such directly warming the ocean surface. Local changes in the energy fluxes could also affect the atmospheric circulation through changes in the position of the Intertropical Convergence Zone (ITCZ) or the West African Monsoon (WAM) affecting TC activity (Schneider et al., 2014; Seth et al., 2019). For these reasons, a better understanding of the role of WAM intensity and dust loading in altering hurricane activity is of paramount importance.

Dramatic intensifications of the WAM have occurred in the past (Shanahan et al., 2009), the most recent during the early and middle Holocene (MH, 12 000 – 5 000 yrs BP) when the WAM was much stronger and extended further inland than today. The northward penetration of the WAM led to an expansion of the North African lakes and wetlands, as well as to an extension of Sahelian vegetation into areas that are now desert, giving origin to the so-called "Green Sahara" (e.g., Holmes, 2008; Kowalski et al., 1989; Rohling et al., 2004). Therefore, the MH climate represents a good test case to investigate the TC response to changes in orbital forcing and also investigate how radiative forcing caused by a greener Northern Hemisphere can impact their genesis.

Paleotempestology records are, however, sparse and most of them only span a few millennia, making it difficult to evaluate TC variability further back than the observational period. Nevertheless, records from western North Atlantic suggest large variations in the frequency of hurricane landfalls during the late Holocene, together with strong positive anomalies in the WAM (Donnelly & Woodruff, 2007; Greer & Swart, 2006; Liu & Fearn, 2000; Toomey et al., 2013).

Only a handful of modeling studies investigating TC changes during the MH are currently available (Korty et al., 2012; Koh & Brierley, 2015; Pausata et al., 2017). Both Korty et al. (2012) and Koh & Brierley (2015) have focused on simulations of the Paleoclimate Modelling Intercomparison Project (PMIP), which only account for the change in orbital forcing and the greenhouse gas concentrations during the MH, assuming preindustrial vegetation cover and dust concentrations. These studies do not explicitly simulate the changes in TCs, but rather investigate how key environmental variables affect TC genesis due to the insolation forcing. Both studies came to similar conclusions that considering changes in the orbital forcing induce changes that make the environment less prone to develop TCs in Northern Hemisphere summer while more prone in the Southern Hemisphere summer. More recently, Pausata et al. (2017) used a statistical thermodynamical downscaling approach (Emanuel et al., 2006, 2008) to generate large number of synthetic TCs and assess their changes during the MH with an enhanced vegetation cover over the Sahara and reduced airborne dust concentrations. Their results suggest a large increase in TC activity worldwide and in particular in the Atlantic Ocean in the MH climate. However, this kind of

downscaling approach does not consider how the TC genesis may have been affected by changes in atmospheric dynamics, such as those associated to the African Easterly Waves (AEWs; Gaetani et al., 2017) that are known to seed TC genesis (Caron & Jones, 2012; Frank & Roundy, 2006; Landsea, 1993; Thorncroft & Hodges, 2001; Patricola et al., 2018). Here, we use the same modeling simulations as in Pausata et al. (2017) to drive a high-resolution regional climate model to investigate the impact of the atmospheric dynamics changes induced by Saharan vegetation and dust reduction on TC activity during the MH compared to the PI climate. This study will compare the dynamical downscaling results to those obtained with the statistical-dynamical downscaling approach used by Pausata et al. (2017), and how they compare with the findings of Koh & Brierley (2015) and Korty et al. (2012). It will also provide insights into how a potential warmer and greener Northern Hemisphere could alter future Atlantic TC activity.

The paper is structured as follows. The model description, experimental design and the analytical tools used in the study are presented in Section 2. Section 3 focuses on 1) the model's response to the changes in climate conditions on TC activity, 2) the seasonal distribution of TCs and 3) their intensity. Discussion and conclusions are presented in Section 4.

2. Model description and methodology

2.1 Models

The simulations carried out by Pausata et al. (2016) and Gaetani et al. (2017) and performed with an Earth System Model (EC-Earth version 3.1) at horizontal resolution of 1.125°x1.125° and 62 levels in the vertical for the atmosphere (Hazeleger et al., 2012), are used in this study to drive a developmental version of the 6th generation Canadian Regional Climate Model (CRCM6; see Girard et al., 2014 and McTaggart-Cowan et al., 2019). The experiments with CRCM6 are carried out on a grid mesh of 0.11°. This high horizontal resolution grid allows to capture many processes that are related to TC genesis and simulate intense tropical cyclones (Strachan et al., 2013; Walsh et al., 2013; Shaevitz et al. 2014; Camargo & Wing 2016; Kim et al. 2018; Wing et al. 2019). CRCM6 is derived from the Global Environmental Multiscale version 4.8 (GEM4.8), an integrated forecasting and data assimilation system developed by the Recherche en Prévision Numérique (RPN), Meteorological Research Branch (MRB), and the Canadian Meteorological Centre (CMC). GEM4.8 is a fully non-hydrostatic model that uses a semi-implicit, semi-Lagrangian time discretization scheme on a horizontal Arakawa staggered C-grid. It can be run either as a Global Climate Model (GCM), covering the entire globe, or as a nested regional climate model (RCM). In the RCM configuration, the model uses a hybrid-terrain-following vertical coordinate with 53 levels topping at 10 hPa. For shallow convection, GEM uses the Kuo transient scheme (Bélair al., 2005; Kuo, 1965) and for deep convective processes, it uses the Kain-Fritsch scheme (Kain & Fritsch, 1990). Finally, CRCM6 is coupled at its lower boundary with the Canadian Land Surface Scheme (CLASS; Verseghy, 2000, 2009) and the lake model Flake (Mironov, 2008; Martynov et al., 2012) to represent the different surfaces. More details regarding GEM4.8 can be found in Girard et al.

(2014). In this study, CRCM6 is integrated on a domain encompassing the Atlantic Ocean from Cape Verde to the North American west coast (~25° W to 120° W and 0° to 45° N; see Fig. 1).

2.2 Experimental design

100   We performed three distinct 30-year long experiments with CRCM6 (see Table 1). The first experiment, the control or reference case, is a pre-industrial climate (PI) simulation that follows the protocol set by the Paleoclimate Modelling Intercomparison Project (PMIP) and the fifth phase of the Coupled Model Intercomparison Project (CMIP5) (Taylor et al., 2012). Two MH simulations were also performed: in the first one the PMIP protocol is followed, only accounting for changes in the orbital forcing (~5% increase in Northern Hemisphere insolation compared to present day values) and the

105   greenhouse gases concentrations (MH_{PMIP}) relative to the PI. The aim here is to evaluate the effect of the insolation forcing alone on TC activity compared to the reference case. In the second MH experiment, in addition to the changes in the MH_{PMIP}, the Sahara Desert (11°–33°N and 15°W–35°E) was replaced by evergreen shrub and airborne dust concentrations reduced by up to 80% in the EC-Earth experiment (MH_{GS+RD}) relative to PI. Due to those changes in vegetation in the Sahara, the albedo of the region decreased from 0.30 to 0.15 and the leaf-area index increased from 0.2 to 2.6 (for details refer to Pausata et al.,

110   2016 and Gaetani et al., 2017). GEM has a basic representation of aerosol accounting for only the extinction coefficient, single scattering albedo and asymmetry factor for continental and maritime particles. These values are spread evenly over the longitudes with higher values at the equator and lower at the poles, and higher values over land than over the ocean. Given such a coarse representation of the aerosol optical properties we did not change them when performing the regional MH_{GS+RD} experiment. Therefore, the major impacts of dust changes in the regional simulation (MH_{GS+RD}) were accounted for through

115   the changes in the prescribed SST and lateral boundary conditions.

2.3 Tracking algorithm

In this study, a storm tracking algorithm was developed using a three-step procedure (*Storm identification, Storm tracking and Storm lifetime*) to detect tropical cyclones, following previous studies (Gualdi et al., 2008; Scoccimarro et al., 2011;

120   Walsh et al., 2007). In comparison to most routines, our algorithm performs a double filtering approach similar to that applied in Caron & Jones (2012) to ensure that the genesis and dissipation phases of TCs are well represented and that TCs are not counted twice in case of a temporary decrease intensity followed by a re-strengthening. Looser detection criteria (with lower values than the standard thresholds values) were first used in order to detect all storm centers, then criteria were enforced to standard values following the literature (strict criteria). Centers that satisfy the strict criteria are then classified as

125   being *strong* centers (*Storm identification*) while the others are classified as *weak* centers. To correctly represent each track (*Storm tracking*), the *strong* and *weak* centers are then paired following two different methods: the *storm history* using a similar approach to that of Sinclair (1997) and the *nearest neighbour* method as in Blender et al. (1997), Blender & Schubert (2000) and Schubert et al. (1998). Once the storm tracks are defined, the algorithm determines the core of each track as the

centers sitting between the first and the last *strong* centers found in the track, thus neglecting the genesis and dissipation

130   phases. This subsection of the track (representing the main TC lifetime) has to satisfy a third set of criteria that reject TCs that do not live long enough, or that do not travel a long enough distance, or that do not reach the strength of a Tropical Storm. If the core of the storm track satisfies all these criteria, the genesis and dissipation phase (represented by the *weak* centers that occurred before the first and after the last *strong* centers) are added to form the complete storm track. A detailed description of the storm identification and tracking can be found in the *Appendix*.

135   **2.4 Potential intensity and genesis indices**

Many environmental proxies have been used to link the changes in the dynamical and thermodynamical fields to TC activity. Here two well-known environmental proxies were adopted, the Potential Intensity (V_{PI}) and the Genesis Potential Index (GPI), to investigate the changes between different climate states in TC achievable intensity and in the areas more prone to develop TCs, respectively. To calculate the theoretical maximum intensity of TCs given specific environmental conditions,

140   the V_{PI} formulation includes the sea-surface temperature (SST), the temperature at the level of convective outflow (T_o), the ratio of drag and enthalpy exchange coefficients ($C_k/C_d = 0.9$), and the available potential convective energy difference between an air parcel lifted from saturation at sea level ($CAPE^*$) at the radius of maximum winds and an air parcel located in the boundary layer ($CAPE_b$). The formula defined by Emanuel (1995) and updated by Bister & Emanuel (1998, 2002) was used to account for dissipative heating:

145   $$V_{PI} = \sqrt{\frac{C_k \cdot SST}{C_d \cdot T_o}(CAPE^* - CAPE_b)} \tag{1}$$

The Genesis Potential Index (GPI) is an empirical fit of the most important environmental variables known to affect TC formation. These variables include dynamical (wind shear and absolute vorticity) and thermodynamical (potential intensity and moist entropy deficit) factors. The first genesis index was introduced by Gray (1975, 1979). Since then, various genesis indices have been formulated (e.g. Emanuel & Nolan, 2004; Emanuel, 2010; Korty et al., 2012). Here the genesis index

150   formulation from Korty et al. (2012) was used, which is a modified version of the GPI index described in Emanuel (2010). This GPI includes the entropy deficit between different atmospheric levels, as the one of Emanuel (2010), with the addition of the «clipped vorticity» (Tippett et al., 2011):

$$GPI = \frac{a[min(|\eta|, 4\times10^{-5})]^3 [max(V_{PI}-35, 0)]^2}{\chi^{4/3}[25+V_{shear}]^4} \tag{2}$$

where V_{PI} is the potential intensity, V_{shear} is the wind shear between 250 and 850 hPa levels, η is the absolute vorticity at

155   850hPa, and a is a normalization coefficient. The entropy deficit χ is defined as:

$$\chi = \frac{s_b - s_m}{s_o^* - s_b} \tag{3}$$

where s_b, s_m and s_o^* represent, respectively, the moist entropies of the boundary layer (900 hPa), middle troposphere (600 hPa), and the saturation entropy at the sea surface. Other indices have shown similar performances to the GPI, as for example the Tropical Cyclone Genesis Index - TCGI (Tippett, et al. 2011; Menkes et al. 2011).

2.5 Regional model evaluation

To evaluate the CRCM6 performance in simulating tropical cyclones, an additional simulation was carried out using the ERA-Interim reanalysis as lateral boundary conditions and SSTs, and compared with 25-km ERA5 reanalysis **data itself** for the period 1980 to 2009 (see Copernicus Climate Change Service (C3S), 2017). Our storm-tracking algorithm was used to detect tropical cyclones in the ERA5 reanalysis, for validation and to ensure the accuracy of simulated results against the observed track density obtained from the Atlantic «Best Track» dataset (HURDAT2) (Landsea & Franklin, 2013) for the same period (1980-2009). The use of the high-resolution ERA5 reanalysis data allowed us to directly compare the obtained results to our modeled 0.22° data and the HURDAT2 observations. The comparison between the detected TCs in ERA5 reanalysis data and the observed TCs from HURDAT2 data base also provided a quick test case to evaluate ERA5 ability to represent observed TCs while using the same detection criteria, which cannot be done with the coarser resolution of the raw ERA-Interim data (~80 km). The model evaluation is presented in the *Appendix*. In general, our tracking algorithm captures well the main characteristics of the observed tracks (Fig. A1). However, the number of detected TCs in ERA5 data is lower than observations, even when considering lower threshold values. On the other hand, when comparing the ERA-Interim-driven model-simulated TCs in the simulation against observations, there is a better agreement in the mean track characteristics and number of Atlantic TCs (Fig. A1A). Murakami (2014) and Hodges et al. (2017) found significant biases in the representation of TCs in various reanalysis datasets, using different tracking algorithms. Although these results strongly stem from the tracking algorithm ability to capture weaker storms, our comparison between the HURDAT2 TC tracks and those obtained with ERA5 reanalysis shows important differences between the two.

In this study, we use a two-tailed Student t test to determine the statistical significance of changes at the 5% confidence level. The significance of the changes in TC frequency has been determined using twice the standard error of the mean (~5% confidence level). The Accumulated Cyclone Energy (ACE; Bell et al., 2000) was also calculated. ACE is defined as the sum of the square of the maximum sustained wind speed (in knots; 1 kt = 0.514 ms^{-1}) higher than 35 kt every 6 h over all the storm tracks. ACE is an integrated measure depending on TC number, intensity and duration, and less sensitive than TC counts to tracking schemes and thresholds (Zarzycki & Ullrich, 2017). Besides the total ACE, the mean ACE per storm was also considered, and ACE per mean storm duration, in order to analyze the contribution of the different components of ACE to the total value.

To evaluate the statistical significance in the difference in TC counts between different climate states is significant, a bootstrap method was used to create 100 randomly selected 30-year samples out of the 40-year (1979 – 2018) distributions of the annual number of observed TCs and ERA5 TCs.

3. Results

In this section, the TCs in the MH and PI climate conditions are studied to evaluate how changes in orbital forcing, dust and vegetation feedbacks impact TC activity in the Atlantic Ocean, by focusing on TC's trajectories and annual frequency (3.1), seasonality (3.2) and intensity (3.3). We also highlight the impacts of such changes on the different variables known to affect TC genesis.

3.1 Change in TC Density and Frequency

The PI climate simulation has a spatial distribution of Atlantic hurricanes that is similar to present climate, where most of the TCs form in the Main Development Region (MDR) and move west-north-westward towards the North American East Coast (Fig. 2B). However, there are fewer TCs in the simulated PI climate than in the present-day climate simulation driven by ERA-Interim (cf. Figs. 2A and A2); this is due to a large extent to the SST cold bias in EC-Earth simulation (~5°C; see Fig. A3). When only the orbital forcing is considered (MH_{PMIP}), there is a northward shift of the Atlantic TC tracks, as well as an eastward displacement of the tracks away from the U.S. east coast at higher latitudes and a small increase in the TC track density relative to the PI experiment (Fig. 2C). This anomaly pattern is similar to that of the MH_{GS+RD} experiment, but the anomalies are notably stronger in the latter simulation (Fig. 2D), extending further north and westward into the Greater Antilles and Gulf of Mexico. The TC northward shift in the MH experiments and the strong eastward shift at higher latitudes are related to both the northward displacement of the ITCZ and the intensification of the WAM relative to the PI simulation (Fig. A4).

The northward shift of the ITCZ in the MH is due to energetic constraints associated with the changes in orbital forcing causing a warming of the NH and a cooling of SH during boreal summer relative to PI (Merlis et al., 2013; Schneider et al., 2014; Seth et al. 2019). The ITCZ is associated with more favorable conditions for cyclogenesis by increasing the ambient vorticity and therefore the TC activity (Merlis et al., 2013). Our analysis shows that the absolute vorticity maximum undergoes a northward shift relative to the control experiment, following the ITCZ displacement (Fig. A5), supporting the northward shift of the TC tracks (Fig. 2C). Higher absolute vorticity values are also found over the Greater Antilles and the western part of the Gulf of Mexico where there is a higher TC occurrence in the MH_{GS+RD} relative to PI.

The northward shift and the increase of TC activity in the MH experiments is also related to the strengthening of the WAM, which amplifies the westerly winds – and the SST anomaly (Fig. A6). Such changes lead to the development of a wind shear pattern anomaly in the MDR, with lower values of wind shear in the central-western region of the MDR and higher values in the eastern side of the MDR relative to PI. Thus, while the area more favorable for TC development is reduced (Fig. A7), the more favorable conditions present on the western side more than compensate the decrease in the east, allowing more cyclones to develop in the MH experiment. In addition to the zonal atmospheric circulation changes, the enhanced northward

penetration of the WAM together with the displacement of the ITCZ leads to a northward shift of the maximum in African Easterly Waves (AEWs) activity in the MH experiments relative to PI (see Fig. A8). The poleward displacement of the AEWs may also contribute to the changes in TC genesis location as they influence the region where TCs develop (e.g., Caron & Jones, 2012).

The vegetation changes and the associated reduction in dust concentrations further strengthen the WAM in the MH_{GS+RD} relative to the MH_{PMIP} experiment (Pausata et al., 2016; 2017), hence amplifying the changes seen in the MH_{PMIP}. Furthermore, the reduction in dust concentration in the MH_{GS+RD} experiment directly affects the SST (Fig. A6B), leading to an environment more prone to develop TCs relative to the MH_{PMIP} and PI simulations. This is consistent with previous studies that found that the Sahara dust layer can have large impacts on TC activity (Evan et al., 2016; Pausata et al., 2017; Reed et al., 2019).

The GPI anomalies of both MH experiments relative to PI closely follow the changes in the atmospheric and oceanic environmental factors that can affect TCs (cf. Figs. 3, A5, A6, A7, A8 and A9). The GPI shows more favorable conditions with higher values of vorticity and SST and lower wind shear values. Similarly to the absolute vorticity field (Fig. A5), the GPI shows a small northward shift relative to the control experiment, thus contributing to the poleward displacement of the TC genesis locations and therefore the the TC tracks (cf. Figs. 3 and Fig. 4).

The largest changes in GPI are seen in the MH_{GS+RD} experiment (Fig. 3B). The greening of the Sahara and the reduced dust concentrations over the Atlantic Ocean not only lead to higher potential for cyclogenesis in the MDR, but also extend the region westward towards the Caribbean where the model simulates a higher occurrence of TCs in this experiment relative to the PI (see Fig. 2C). Overall, the changes in cyclogenesis density for both MH experiment follow closely the changes in GPI (cf. Figs. 3 and 4), suggesting that GPI is a good predictor of the TC activity changes, even in very different climate states. Moreover, in Pausata et al. (2017), the TC genesis anomalies in the MH experiments show a westward shift, while in our analysis the TC genesis anomalies relative to PI present a net northward displacement of its locations, highlighting an important difference between the two downscaling techniques (see Fig. A10). These changes in the TC genesis are likely responsible for the downstream changes in the TCs track density in both studies.

In terms of frequency, an average of 5.5 TCs per year is simulated in the PI experiment (Fig. 2B). This is ~45% less than the present-day climatology (~10 TCs per year; Landsea, 2014), which is likely due to a strong cold bias in the SST of the coupled model simulation (see Fig. A3 and Pausata et al., 2017). Many high-resolution global models have similar biases in the Atlantic (e.g. Shaevitz et al., 2014; Wing et al., 2019). The MH_{PMIP} experiment shows a small increase (+9%; statistically significant) in the TC frequency relative to the PI, highlighting the minor impact of the orbital forcing alone on the number of Atlantic TCs (Fig. 2B). In the MH_{GS+RD} simulation, more TCs are generated (7 per year) with a significant increase of

around 1.5 TCs per year (+27%) relative to the PI experiment (Fig. 2B). Bootstrap tests with both HURDAT2 (Fig. 5A) and ERA5 (Fig. 5B) datasets show that the chances of obtaining an increase of 27% (9%) in the mean of each distribution are significantly (slightly) higher than the 95th percentile of these distributions. Our sensitivity experiments hence roughly show that the orbital forcing alone contributes for about 33% (~0.5 TC per year) of the total increase in TC frequency occurring in the MH_{GS+RD} relative to the PI experiment, while the Sahara greening and reduced dust concentrations account for about 66% of this increase (~1 TC per year). Thus, these results suggest that the TC activity is strongly dominated by the vegetation and dust changes, in close agreement with Pausata et al. (2017).

3.2 Changes in TC Seasonal Cycle

To analyze changes in TC seasonal cycle we consider changes in the monthly number of TCs, rather than change of the length of the TC season. The PI climate has a TC seasonal cycle that is similar to the present climate, with a peak in TC in September (Fig. 6). The MH experiments show a distinct pattern: a decrease in TC activity at the beginning of the hurricane season for both MH experiments (statistically significant for the MH_{PMIP} in July and August; non-significant for the MH_{GS+RD}), followed by a large increase at the end of TC season (statistically significant during September and October in the MH_{PMIP}; MH_{GS+RD} from September to November, SON) relative to PI.

Gaetani et al. (2017), using the same global model experiments performed with EC-Earth, showed a large decrease in the AEWs in the MH_{GS+RD} relative to the MH_{PMIP} simulation due to the strengthening of the WAM. As AEWs can potentially act as seeds for TC genesis (Caron & Jones, 2012; Frank & Roundy, 2006; Landsea, 1993; Thorncroft & Hodges, 2001), we analyze the changes in the AEW seasonality in the MH experiments relative to PI to determine whether there is a direct link between the changes in the seasonality of AEW and TCs (Fig. 7). The AEWs activity is remarkably reduced between July to September – 80% less relative to PI – and intensified in October and November in the MH_{GS+RD} relative to PI (Fig. 7B).

The reduction of the AEWs in the MH_{GS+RD} experiment is related to the strengthening and northward shift of the West African Monsoon (WAM). The anomalous westerly wind flow associated with the northward expansion of the WAM rainfall significantly alters the African Easterly Jet (AEJ) (Fig. 8) and the Sahara Heat Low. In particular, the disappearance of the 600 hPa AEJ and northward displacement of the wind circulation is responsible for the lower frequency of AEWs during the summer months in the MH_{GS+RD} relative to PI. On the other hand, the withdrawal phase of the WAM towards the end of the season (SON) is associated with an increase in the frequency of AEWs relative to PI, potentially contributing to the increase in TC activity in those months. While the changes in the frequency of AEWs in the MH_{GS+RD} are potentially in agreement with the simulated changes in TC seasonality, the frequency of AEWs in the MH_{PMIP} is higher relative to PI, especially in June and July, which is at odds with the changes in TC frequency in the MH_{PMIP} experiment (no change in June and slightly decrease in July; Fig. 7A). Furthermore, in July and August fewer TCs are simulated in the MH_{PMIP} relative to the MH_{GS+RD}, which has fewer AEWs. Hence, it is not possible to draw a direct link between the changes in the seasonality

290 of AEWs and TCs between the MH and the PI simulations. These results agree with the findings of Patricola et al. (2018) that, while AEWs can affect TC genesis, their contribution may not be necessary and TCs can also be formed from other processes such as wave breaking of the ITCZ, disturbance from Asian monsoon trough or self-aggregation of convection (Patricola et al., 2018). Furthermore, Vecchi et al. (2019) showed that a combination of the large-scale environmental factors (in particular ventilation) and the frequency of disturbances determined the TC frequency in their model.

295

Other factors could be playing a role in modifying the TC seasonal cycle. In particular, the shift in TC seasonal cycle could be related to changes in the orbital forcing, most importantly the precession of the equinoxes: during the MH the perihelium was in September instead of January as today, with the stronger insolation anomalies peaking in late summer at NH low latitudes. Furthermore, while higher potential intensity (due mostly to warmer SSTs, see Figs. A6 and A11) develops on the

300 western part of the MDR and most of the North Atlantic Ocean from June to September relative to the PI experiment, the strengthening of the WAM causes a cold anomaly response over the eastern part of the MDR, together with stronger vertical wind shear and weaker absolute vorticity values. The withdrawal of the WAM in late September then causes the decrease in wind shear, and positive anomalies in both absolute vorticity and SSTs to extend eastward. These environmental anomalies are likely the reason for the TC seasonality changes during the MH experiments (Fig. A11A, A12A, A13A). The

305 cyclogenesis anomalies and the GPI changes are consistent with these assumptions (cf. Figs. 9A and A14A). Korty et al. (2012), who studied the response to orbital forcing in PMIP2 models during the MH, also found that the TC season in the Northern Hemisphere was less favorable during summer while become more favorable during fall (October and November) relative to pre-industrial climate. The authors pointed out that these findings were due to the difference between the warming rate of the atmosphere (which warm faster during the summer months) and that of the ocean surface, who led to a negative

310 potential intensity anomaly during the first half of their TC season (June to September) and a positive anomaly during the second half (October to November). Using PMIP3 models, Koh & Brierley (2015) drew similar conclusions; however, the changes in fall were not a robust signal across models.

Accounting for the Sahara greening and reduced airborne dust concentrations (MH$_{GS+RD}$) leads to even larger changes

315 relative to PI (Fig. A11B, A12B, A13B), strengthening the GPI anomalies in the MDR (Fig. 9B). These changes strongly increased the total GPI over the ocean from September to November in the MH$_{GS+RD}$ experiment and lead to almost twice as many cyclones in November relative to PI and MH$_{PMIP}$ experiments (see Figs. 6, 10 and Fig. A14B). Furthermore, there is a westward extension of the region prone to TC development towards the Greater Antilles and the Caribbean Sea from July to September relative to the other two experiments (Fig. 9B and Fig. 11), which is also reflected in the seasonal GPI (Fig. 3B).

320 These anomalies led to a small increase in cyclogenesis over the Caribbean Sea relative to PI during this part of the season and may explain the increased TC activity during July and August in the MH$_{GS+RD}$ relative to the MH$_{PMIP}$ and why almost as much cyclones formed during September (cf. Figs. 6, A14).

3.3 Changes in Intensity

To assess TC intensity, we considered the 10-m maximum wind speed in 3 h intervals and then classified them using the Saffir-Simpson scale categories. For the three experiments, most tropical cyclones reach only tropical storm or hurricane Category 1 (93%, 88% and 91% for PI, MH_{PMIP} and MH_{GS+RD}, respectively) with only a few reaching Category 2 (7%, 11% and 8%) (Fig. 12). Both MH simulations generated Category 3 hurricanes (~1% in both cases), while there are no major hurricanes in the PI experiment. Our analysis of the ACE also reveals that in general, the mean ACE per cyclone in the MH experiments is higher than in the PI experiment (~$6.6x10^4$ m^2s^{-2} and ~$7.4x10^4$ m^2s^{-2} for MH_{PMIP} and MH_{GS+RD}, respectively, ~$6.1x10^4$ m^2s^{-2} for PI; see legend in Fig. 13C). The increase in ACE in MH simulations arises from two different aspect: (1) TCs in the MH climate are more intense than in the PI experiment (as shown in Fig. 12), therefore leading to higher rate of energy generation, and (2) TCs in the MH experiments tend to last longer (PI: 199 h, MH_{PMIP}: 217 h and MH_{GS+RD}: 283 h; see legend Fig. 13C), meaning that the same amount of energy can be spend over a longer time lapse. The combination of these two aspects with increased mean TC count per season in the MH experiments (Fig. 2B and Fig. 14A) therefore leads to a larger total mean ACE per experiment in the MH simulations compared to PI (see legend Fig. 13B).

To better understand the cause of these changes, we turn to the seasonal V_{PI} (Fig. 14) and examine the regions where the atmospheric conditions are more favorable for TC intensification. The area showing the most favorable conditions for cyclone intensification in the MH_{PMIP} relative to the PI experiment is located around the central-western portion of MDR and extends northwards over the central Atlantic Ocean and westward along the northern most part of the US East Coast (Fig. 14A). Less favorable conditions are present east and south of the MDR where colder SSTs are present. The mean V_{PI} pattern for the MH_{GS+RD} yields even stronger anomalies than the ones simulated by the MH_{PMIP}, with substantially more favorable conditions for intensification in the MDR (Fig. 14B). More conducive conditions are also present in the Caribbean Sea where markedly lower values of vertical wind shear are simulated (Fig. A7). The combination of more favorable environmental conditions (e.g. wind shear) along with the occurrence of more TCs crossing this areas in the MH_{GS+RD} experiment relative to both PI and MH_{PMIP} (see Fig. 2D) increases the chances of getting more intense and long-living cyclones. The main factors contributing to the increase in V_{PI} in the MH_{GS+RD} relative to the PI and MH_{PMIP} experiments are the warmer SSTs (~1.5°C higher; Fig. A6B) and enhanced levels of convective available potential energy (CAPE; Fig. A15) as direct consequence of the reduced dust emissions. In comparison to the change seen in the MH_{PMIP} relative to PI, less favorable conditions for intensification are simulated north of the MDR in the MH_{GS+RD} (Fig. 14B). Over all, the V_{PI} anomalies for both MH experiments strongly resemble those presented in Pausata et al. (2017) and closely follow the changes in GPI, therefore leading to more intense and potentially longer-living cyclones where better conditions are available for cyclogenesis.

4. Discussion and Conclusions

In this study, we use the regional climate model CRCM6 with a high horizontal resolution (0.11°) to better investigate the role played by vegetation cover in the Sahara and airborne dust on TC activity in the Atlantic Ocean during a warm climate period, the mid-Holocene (MH, 6,000 yrs BP). We compared two different MH experiments – where only orbital forcing is considered (MH_{PMIP}) and where also changes in vegetation and dust concentration are accounted for (MH_{GS+RD}) – to a control pre-industrial experiment (PI). Our results show that the Sahara greening and related reduction in dust concentrations (MH_{GS+RD} experiment) significantly increase the number of TC in the North Atlantic Ocean by about 27%, whereas the increase associated with the orbital forcing alone is smaller (9%; MH_{PMIP}). In general, our results are consistent with the findings of Pausata et al. (2017), who used the same coupled global model simulation to drive a statistical–thermodynamical downscaling technique (Emanuel et al., 2008) to assess changes in TC activity; however, the changes in TC activity simulated in our study between the MH experiments and the PI simulation are smaller. Furthermore, the displacement of TC activity is different in our study (meridional vs. zonal) and most likely related to the fact that dynamical changes in ITCZ and AEW are not accounted for in Pausata et al. (2017). Our experiments show that the MH climate induces a northward shift of the North Atlantic TC tracks and an eastward displacement of those away from the U.S. east coast at higher latitudes. A zonal shift of the storm track relative to PI is instead simulated in Pausata et al. (2017). Our work also suggests an important reduction of the TC activity during the first half of the TC seasonal cycle in the MH experiments together with a shift of the maximum TC activity towards the second half.

Gaetani et al. (2017) showed a strong decrease in AEW in the MH_{GS+RD} simulations and suggested a potential impact in TCs activity; however, our analysis does not show a consistent relationship between the frequency of AEWs and tropical cyclones. These results support the findings of Patricola et al. (2018) who showed through a set of sensitivity experiments that the AEWs may not be necessary for TC genesis as TC formation occurs even in the absence of AEWs through other mechanisms. This is supported by observational studies that could not find a direct relation in the frequency of AEWs and TCs (Russell et al., 2017). Instead, the AEWs seem to play a more important role on the location of TC genesis rather than the total TC frequency. Furthermore, the RCM domain size and location of the lateral boundary conditions impacts the frequency of AEWs TCs inside the domain (Caron & Jones, 2012; Landman et al., 2005).

Our study suggests that the different orbital parameters together with the changes in the WAM intensity may have been the main causes of the changes in TC seasonality, offering better conditions for cyclogenesis towards the end of the hurricane season. WAM intensity affects the wind shear in eastern side of the MDR. The WAM withdrawal towards the end of the summer extended the more favourable conditions from the central western portion towards the eastern portion of the MDR, causing an increase in TC activity during the second half of the season in the MH simulations. These results are consistent with the findings of Korty et al. (2012) who also showed higher cyclogenesis potential towards the end of the PI hurricane

season in their MH experiment, with likely increase in TC activity during October when the GPI is at its maximum. However, their results are based on the entire Northern Hemisphere while here we only focus on the North Atlantic Ocean. In addition, our results well compare to those of Koh & Brierly (2015) who found less favorable environmental condition for TC development during Northern Hemisphere summer in the MH relative to pre-industrial when analyzing PMIP3 model

390 simulations. Hence, the impact on TCs of changes in orbital forcing is consistent across different models and highlight an interesting point where there may be a repression of the modeled environmental conditions that negatively affects proxies associated with TC (i.e. the V_{PI} and GPI) and supports these results during the summer months which is later offset by opposite changes during the autumnal season in many of them. Moreover, even if airborne dust variations are dominant in controlling the TC annual total, the orbital forcing has still a detectable role in affecting TC activity. Our work also shows

395 that the GPI is able to represent the regions more prone to TC development in different climate states, in agreement with previous studies (Camargo et al., 2007; Koh & Brierley, 2015; Korty et al., 2012b; Pausata et al., 2017). The reduced dust emissions in the MH_{GS+RD} experiment induces an additional SST warming that enhances the available thermodynamic energy, increasing the VPI even further compared to the MH_{PMIP} and PI experiments, and thus leading to more intense TCs. This SST warming induced effect is consistent with the model-based projections for TC intensity in a warmer future climate

400 (Knutson et al., 2013; Walsh et al., 2016; Knutson et al., 2020).

Finally, the simulated impact of dust changes needs further investigation, as rainfall in the northern Africa can be strongly affected by the dust optical properties (e.g., "heat pump" effect where the atmospheric dust layer warms the atmosphere enhancing deep convection and intensifying the WAM; see Lau et al., 2009). In particular, in EC-Earth dust particles are

405 moderately to highly absorbing particles (single scattering albedo $\omega_0 < 0.95$) with $\omega_0 = 0.89$ at 550 nm. Such a value is too absorbing compared to observations (see figure 1 in Albani et al., 2014) and consequently the radiative impact of dust may well be overestimated. In a recent study, Albani and Mahowald (2019) showed how different choices in terms of dust optical properties and size distributions may yield opposite results in terms of rainfall changes. However, in the EC-Earth simulations most of the changes in the WAM intensity were associated to changes in surface albedo due to greening of the

410 Sahara, which was enhanced by dust reduction through a further increase in surface albedo. This response is opposite to what one would expect from a reduced "heat pump" effect (decreased rainfall), suggesting that the "heat pump" effect is overwhelmed by the changes in surface albedo under green Sahara conditions in EC-Earth simulations. Another important aspect that was not considered in our study are dust-cloud interactions which may further feedback in TC activity, both directly in the TC formation, as well as indirectly by affecting the intensity of the WAM. A recent study (Thompson et al.

415 2019) showed that this interaction could indeed influence the WAM rainfall. Therefore, additional studies investigating the impact of dust optical properties and dust-cloud interactions on TC activity are needed.

In conclusion, our study highlights the importance of vegetation and dust changes in altering TC activity and calls for additional modeling efforts to better assess their role on climate. For example, employing regional model simulations with

420 atmosphere and ocean coupling will be important to better represent the interactions between TC activity and TC-ocean feedbacks as large amount of energy is transferred through TC activity between the atmosphere and the ocean (Scoccimarro et al., 2017). Furthermore, to validate the model results, additional new paleotempestology records across the Gulf of Mexico and Caribbean Sea will be of paramount importance. While our study shows an increase in TC frequency and intensity during a climate state with warmer summers and a stronger WAM, it is difficult to draw a direct conclusion for the future as

425 environmental proxies associated with TCs (i.e. the V_{PI} and GPI) are less sensitive to temperature anomalies caused by CO_2 than by those caused by orbital forcing (Emanuel & Sobel, 2013). However, in the view of a potential future "regreening" of the Sahel and/or reduced Sahara dust layer, as shown in Biasutti (2013), Evan et al. (2016) and Giannini & Kaplan, (2019), our work suggests that these changes may further enhance TC frequency due to only greenhouse gases, in particularly over the MDR, the Greater Antilles and the western portion of the Gulf of Mexico, and could generate more intense and

430 potentially longer-living cyclones, increasing the vulnerability of society to damages from severe TCs.

Appendix

Tracking algorithm

In this study, we developed a tracking algorithm that makes use of a three-step procedure to detect cyclones, following previous studies (Gualdi et al., 2008; Scoccimarro et al., 2011; Walsh et al., 2007):

Storm identification

The storms are identified with the following criteria:

a. The surface pressure at the center must be lower than 1013 hPa and lower than its surrounding grid boxes within a radius of 24 km ($2\Delta x$); this pressure is then taken as the center of the storm.

b. The center must be a closed pressure center so that the minimum pressure difference between the center and a circle of grid points in a small and a large radius around the center (200 km & 400 km radii) must be greater than 1 hPa and 2 hPa respectively.

c. There must be a maximum relative vorticity at 850 hPa around the center (200 km radius) higher than 10^{-5} s^{-1}.

d. The maximum surface wind speed around the center (100 km radius) must be stronger than 8 m/s

e. To account for the warm core, temperature anomalies at 250, 500 and 700 hPa are calculated, where each anomaly is defined as the deviation from a spatial mean over a defined region. The sum of the temperature anomalies between the three levels must then be larger than 0.5 °C.

f. If there are two centers nearby, they must be at least 250 km apart from each other, otherwise the stronger one is taken.

To identify the genesis and dissipative phases of the TCs, a double filtering approach was used, similar to that applied by Caron and Jones (2012). The aforementioned threshold values were used to first detect all the potential centers that could belong to a storm for each time step. Then, these criteria were enforced to the standard values (defined below) following the literature (Gualdi et al., 2008; Scoccimarro et al., 2011; Walsh, 1997; Walsh et al., 2007), and these new threshold values were applied to each center to identify the ones that satisfied these enforced criteria among the potential weak ones pre-defined. The centers that satisfied the standard criteria were labeled by the algorithm as being strong centers (or real TC centers) while those who only satisfied the first set of criteria were identified as being weak centers (with standard values properties defined below).

The enforced criteria are the following:

a. Surface pressure at the center deeper than 995 hPa

b. Minimum pressure difference between the center and a 200 km and 400 km radius greater than 4 hPa and 6 hPa, respectively.

c. Relative vorticity maximum larger than 10^{-4} s^{-1}

d. Wind speed maximum above 17 m/s

e. Warm core temperature anomaly above 2°C

465   Another condition was added that only the strong centers needed to satisfy:

       f.   The maximum wind velocity at 850 hPa must be larger than the maximum wind velocity at 300 hPa.

In doing so, we avoided double counting cyclones that may decreased in intensity, before re-intensifying. Conditions e. and f. are the main conditions that filtered the TCs centers from other low-pressure systems and extratropical cyclones, as TCs have a warm core in their upper part and stronger low-level wind speed than other storms.

470   *Storm tracking*

Storms were then tracked as follow: for each potential center found, the algorithm used the *nearest neighbor* method, also applied in many other studies (Blender et al., 1997; Blender & Schubert, 2000; Schubert et al., 1998), to find a corresponding center in the following 3 h time interval within a 250 km radius around the storm center. Once two centers were paired, they formed a storm track. The potential position of the next center to be a continuation of the storm was then calculated using the

475   storm history, based on the position of the previous two centers, which allowed to establish a possible speed and direction for the predicted center. A similar procedure was applied in Sinclair (1997) and was derived from Murray & Simmonds (1991). The algorithm then searches around the last storm center using the nearest neighbor method and around this potential position at the next time step to find a matching center. The nearest center was always chosen first.

  Storm lifetime

480   Once a track was completed, it had to satisfy the last following conditions:

    1.   The TC had to exist for at least 36 hours (with a minimum of 12 centers at 3 h intervals)

    2.   The TC needed to have at least 12 strong centers along its entire track, so that the shortest TC had only strong centers (36 h)

    3.   The TC had to travel at least 10 degrees (~1000 km) of combined longitude and latitude in its lifetime

485   4.   The number of strong storm centers needed to represent at least 77% of a sub-part of the complete storm track delimited by the first and last strong center found by the algorithm. This way, we ensured that the storm was most of its time classified as a TC.
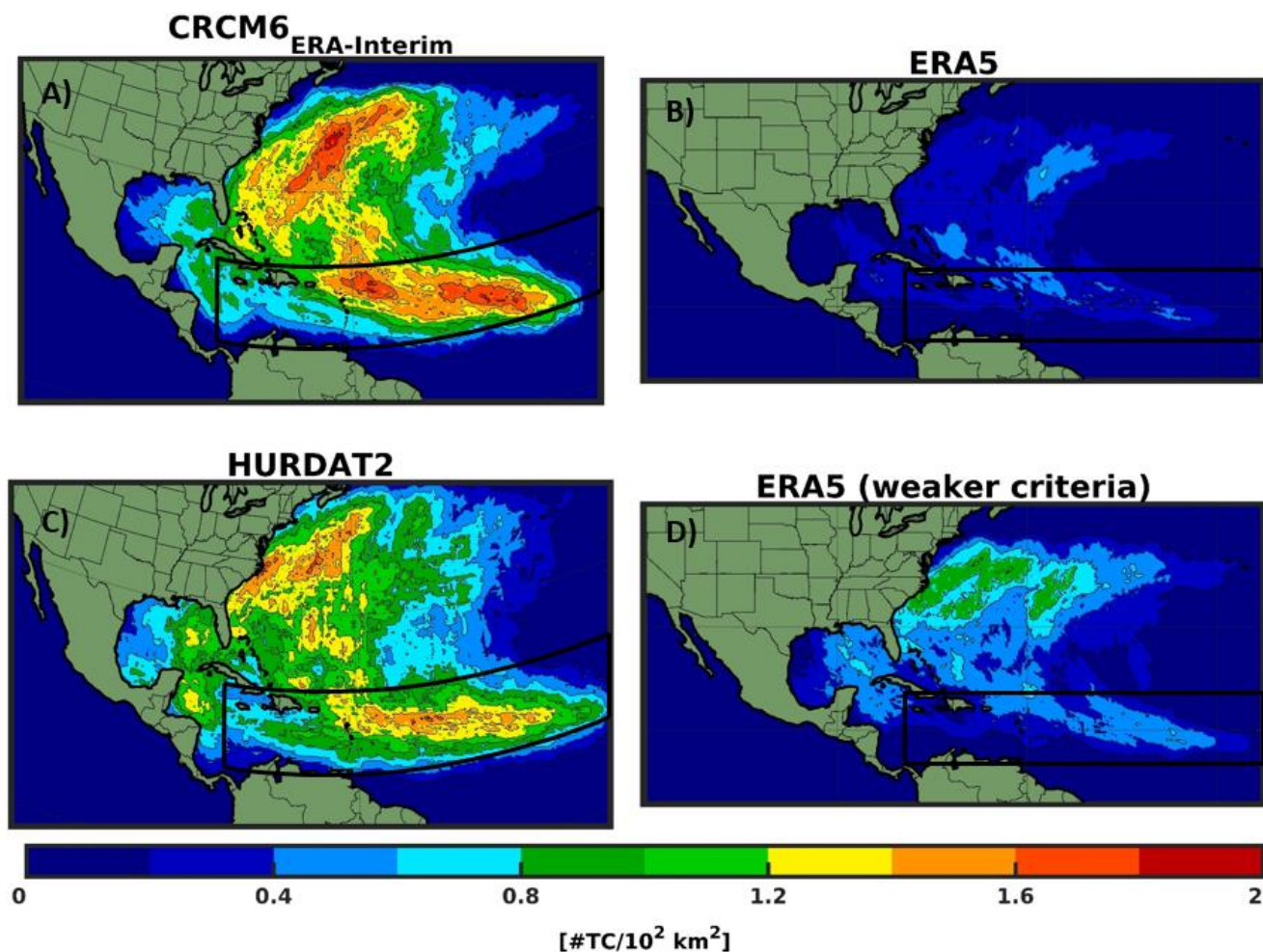
Figure A1: June to November (JJASON) climatology (1980-2009) of (A) track density for the CRCM6 ERA-Interim driven experiment at 0.22°; B) ERA5 reanalysis data at 0.25°; C) Observed TCs from the HURDAT data base at 0.11° and D) ERA5 reanalysis data using weaker detection criteria at 0.25°. The black box shows the present-day Main Development Region (MDR). Note that the ERA5 figures are projected over a Mercator grid while the other two figures use the Equidistant Cylindrical Projection. The contour lines follow the colorbar scale.
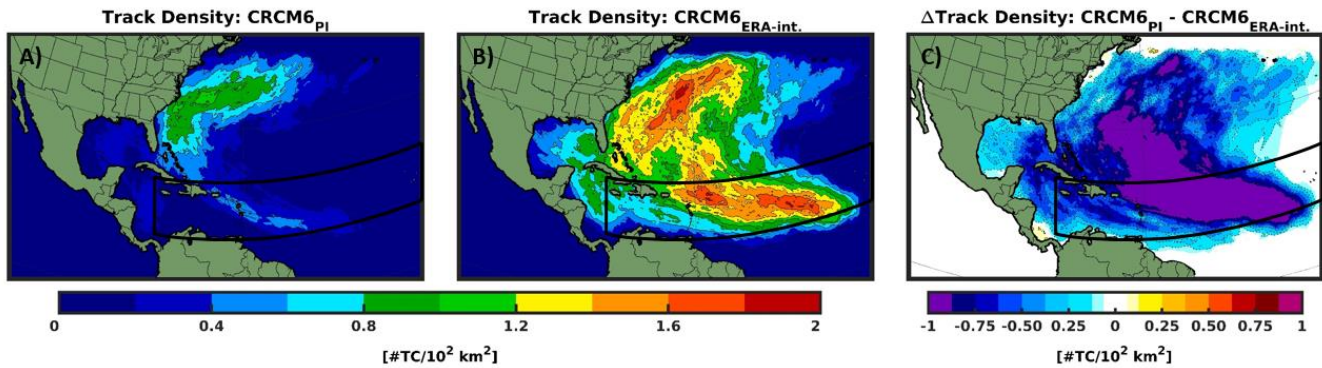
Figure A2: Climatological track density (JJASON) for (A) pre-industrial experiment and (B) ERA-Interim driven experiment. (C) Changes in track density between the two simulations. The black box shows the approximate present-day Main Development Region (MDR). Only values that are significantly different at the 5% level using a local (grid-point) *t* test are shaded. The contour lines follow the colorbar scale (dashed, negative anomalies; solid, positive anomalies); the 0 line is omitted for clarity.

505
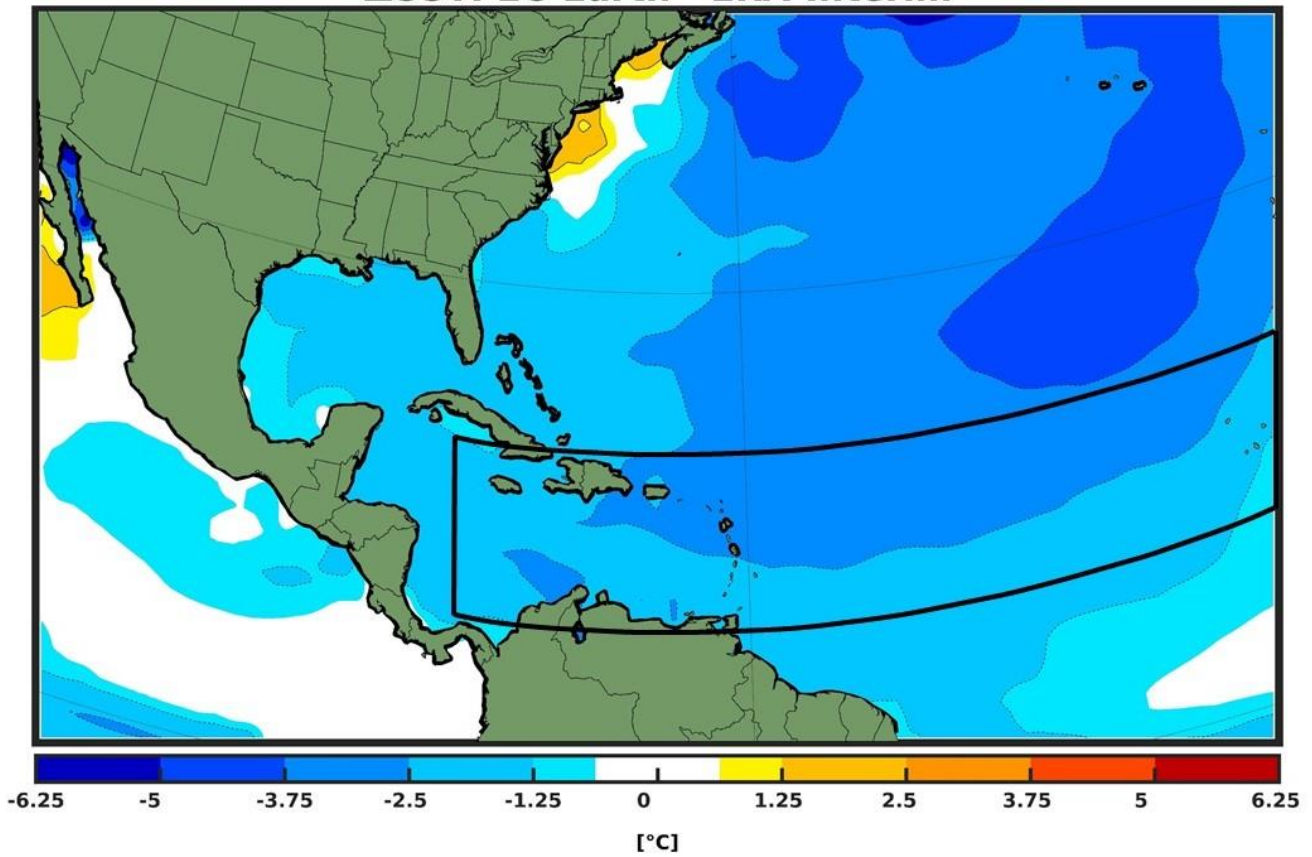
Figure A3: Climatological changes in Sea Surface Temperature (SST) between simulated EC-Earth preindustrial climate and ERA-Interim reanalysis from 1979 to 2008. The black box shows the approximate present-day main development region (MDR). The contour lines follow the colorbar scale (dashed, negative anomalies; solid, positive anomalies); the 0 line is omitted for clarity.
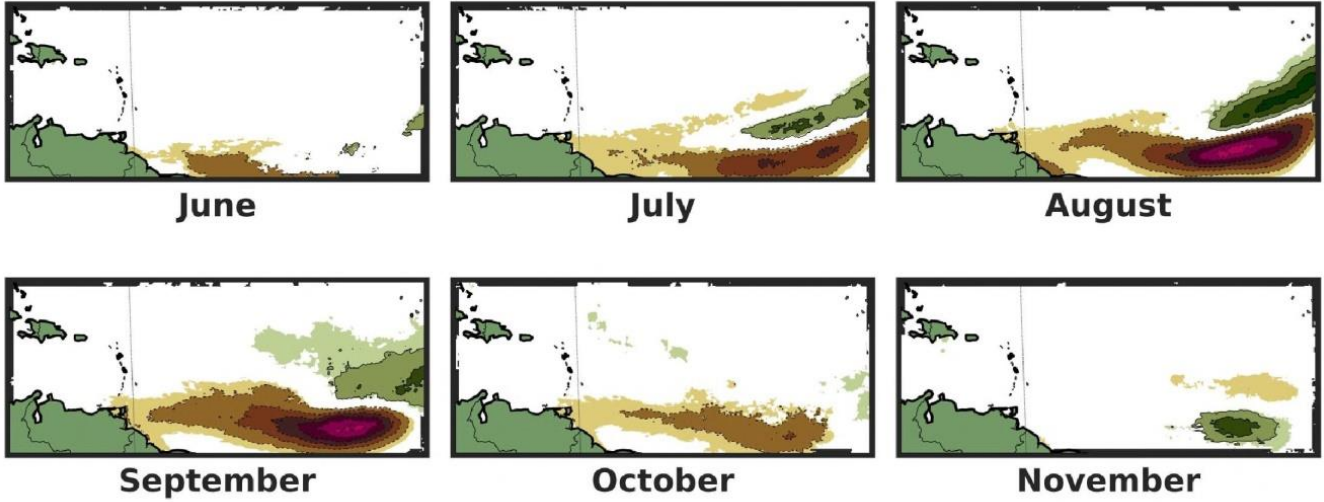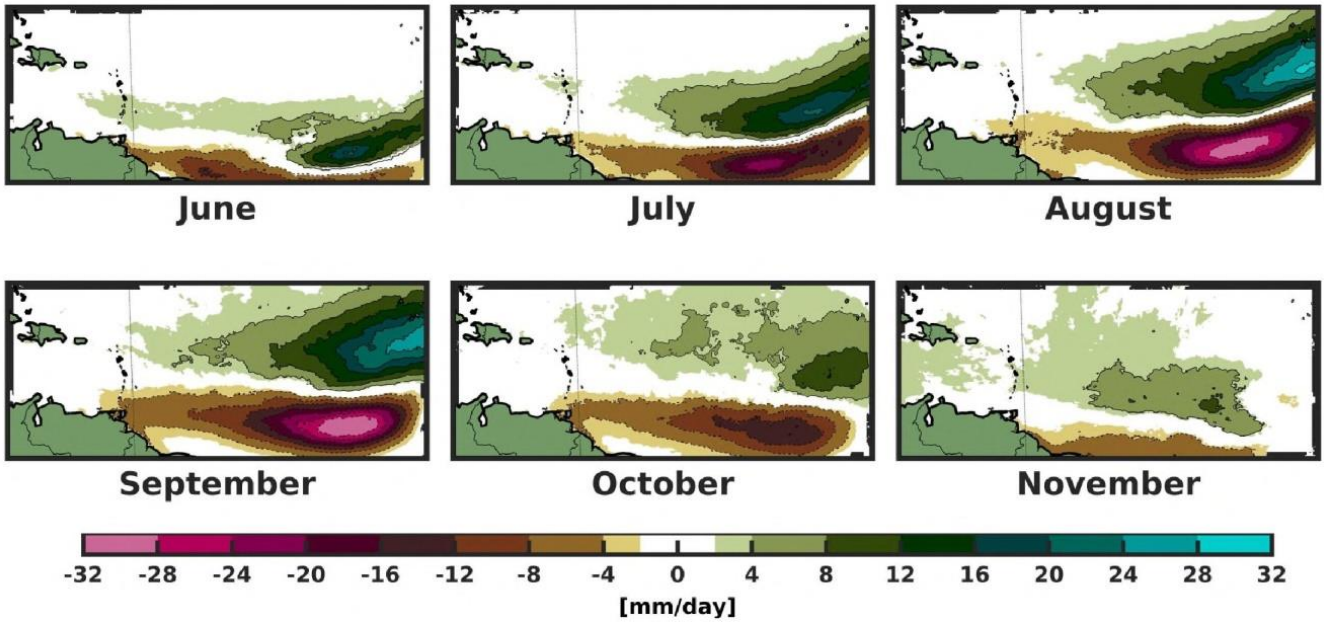
Figure A4: Monthly mean climatological changes in precipitation for (A) MH_{PMIP} and (B) MH_{GS+RD} relative to PI in the domain 23° W-75° W, 5° N-23° N. Only values that are significantly different at the 5% level using a local (grid-point) *t* test are shaded. The contour lines follow the colorbar scale (dashed, negative anomalies; solid, positive anomalies). The 0 line is omitted for clarity.
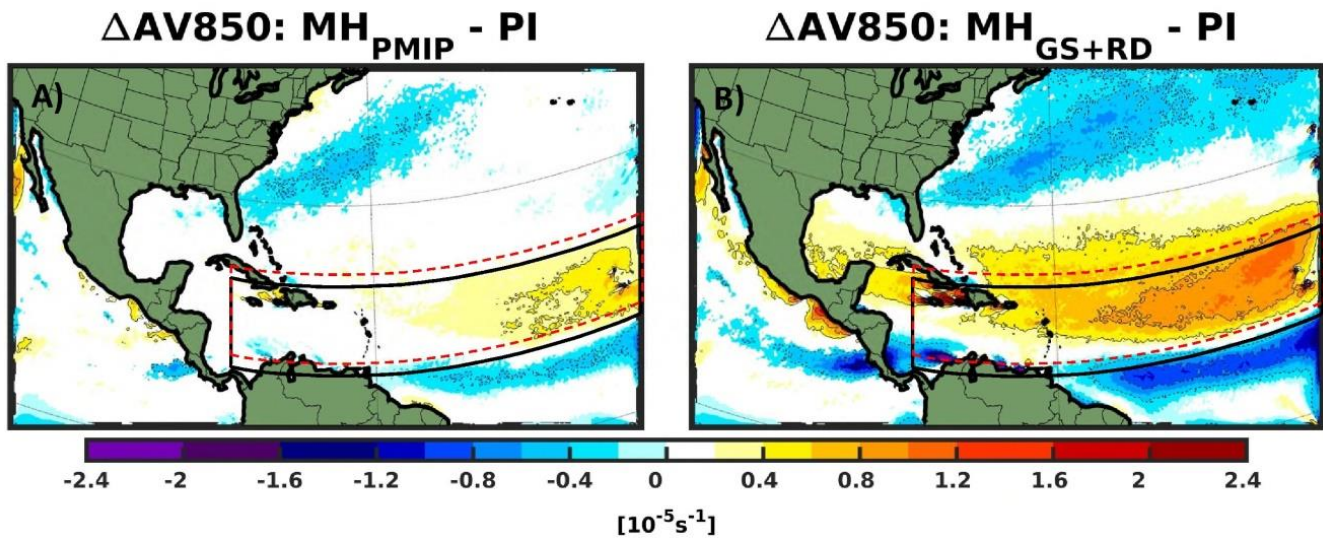
520 **Figure A5:** Climatological (June to November, JJASON) changes in 850 hPa absolute vorticity relative to PI for (A) MH$_{PMIP}$ experiment and (B) MH$_{GS+RD}$ experiment. The black box represents the approximate present-day MDR. Red dotted box shows the approximate shift in the absolute vorticity maxima. Only values that are significantly different at the 5% level using a local (grid-point) t test are shaded. The contour lines follow the colorbar scale (dashed, negative anomalies; solid, positive anomalies); the 0 line is omitted for clarity.

525
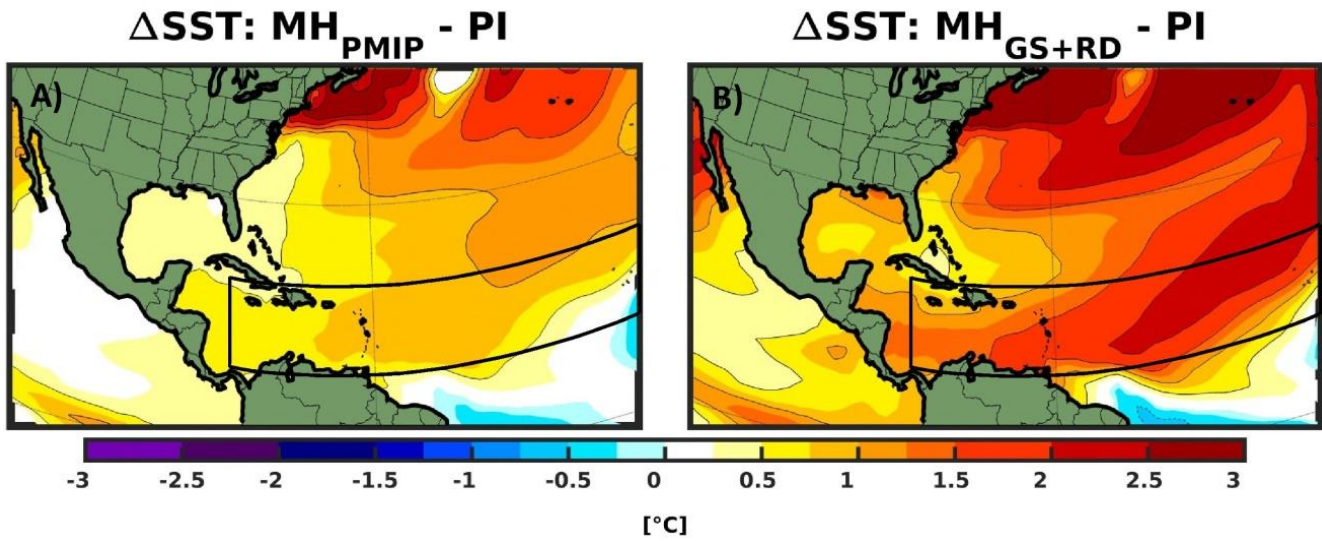
Figure A6: Climatological (JJASON) changes in Sea Surface Temperature (SST) for (A) MH_{PMIP} and (B) MH_{GS+RD}
experiments relative to PI. The black box shows the approximate present-day Main Development Region (MDR). Only
values that are significantly different at the 5% level using a local (grid-point) t test are shaded. The contour lines follow the
colorbar scale (dashed, negative anomalies; solid, positive anomalies); the 0 line is omitted for clarity.
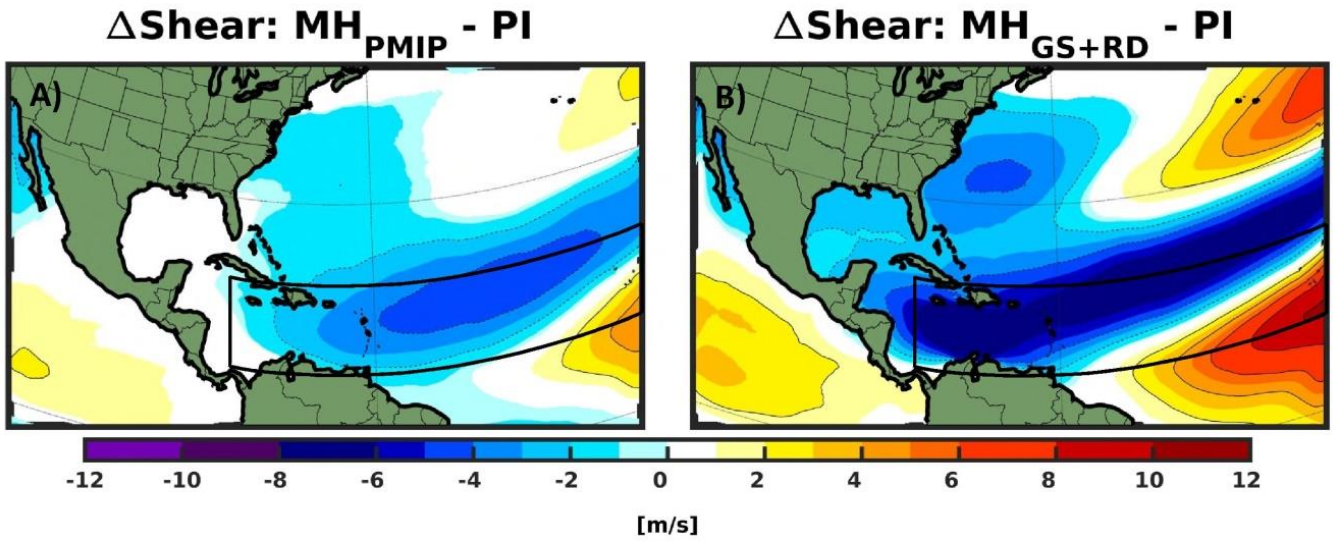
535 **Figure A7:** Changes in vertical wind shear (300 hPa – 850 hPa) for (A) MH$_{PMIP}$ and (B) MH$_{GS+RD}$ experiments relative to PI. The black box shows the approximate present-day Main Development Region (MDR). Only values that are significantly different at the 5% level using a local (grid-point) t test are shaded. The contour lines follow the colorbar scale (dashed, negative anomalies; solid, positive anomalies); the 0 line is omitted for clarity.
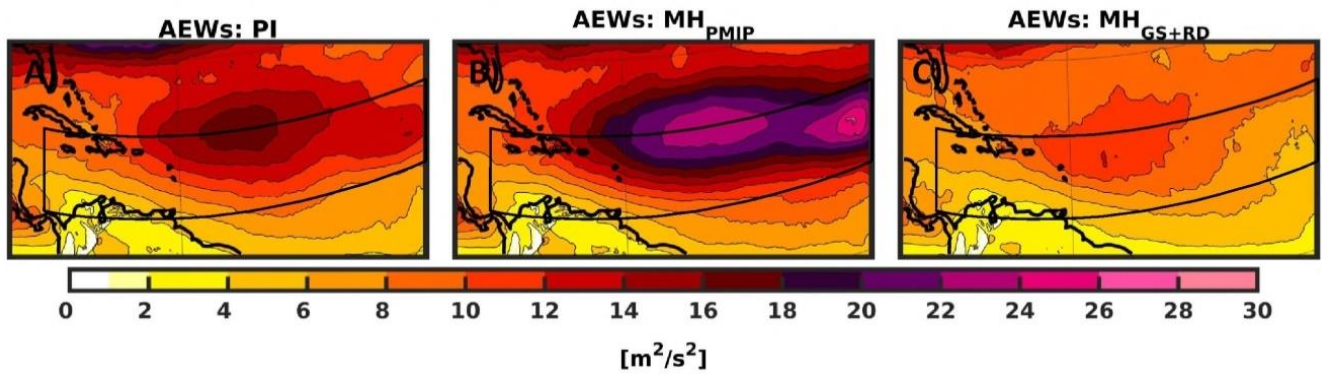
Figure A8: African Easterly Waves represented through the variance of the meridional wind at 700 hPa, filtered in the 2.5- to 5-day band, for (A) PI, (B) MH$_{PMIP}$ and (C) MH$_{GS+RD}$ experiments. The black box shows the approximate present-day Main Development Region (MDR). The contour lines follow the colorbar scale.

540
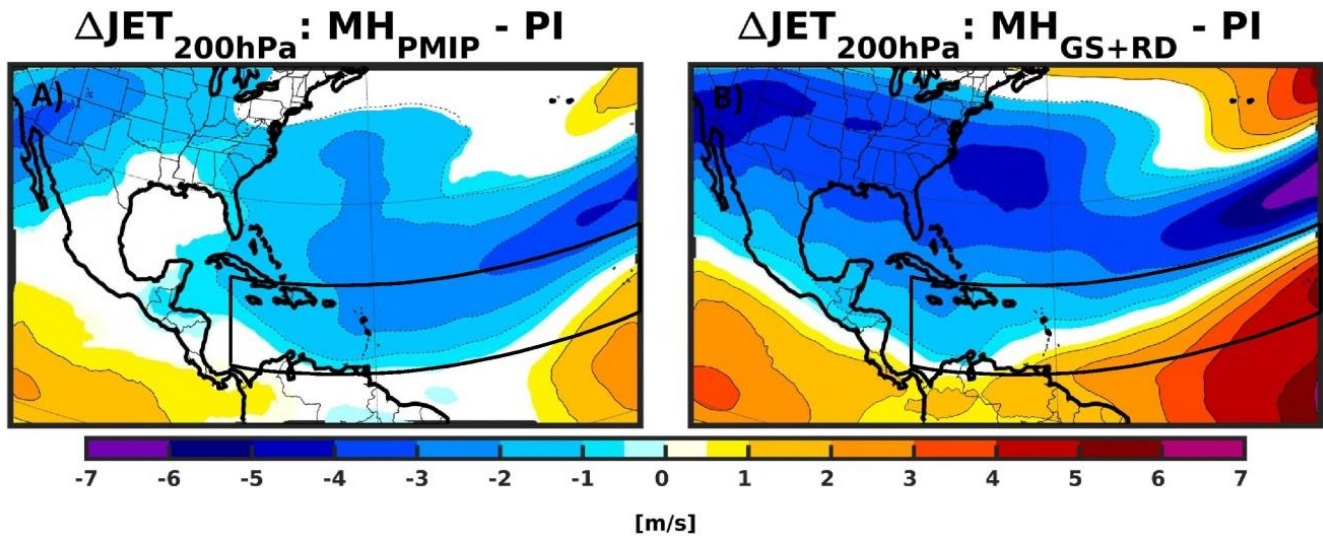
545

Figure A9: Climatological (JJASON) changes in 200 hPa wind speed for (A) MH_PMIP and (B) MH_GS+RD experiments relative to PI. The black box shows the approximate present-day Main Development Region (MDR). Only values that are significantly different at the 5% level using a local (grid-point) t test are shaded. The contour lines follow the colorbar scale (dashed, negative anomalies; solid, positive anomalies); the 0 line is omitted for clarity.

550
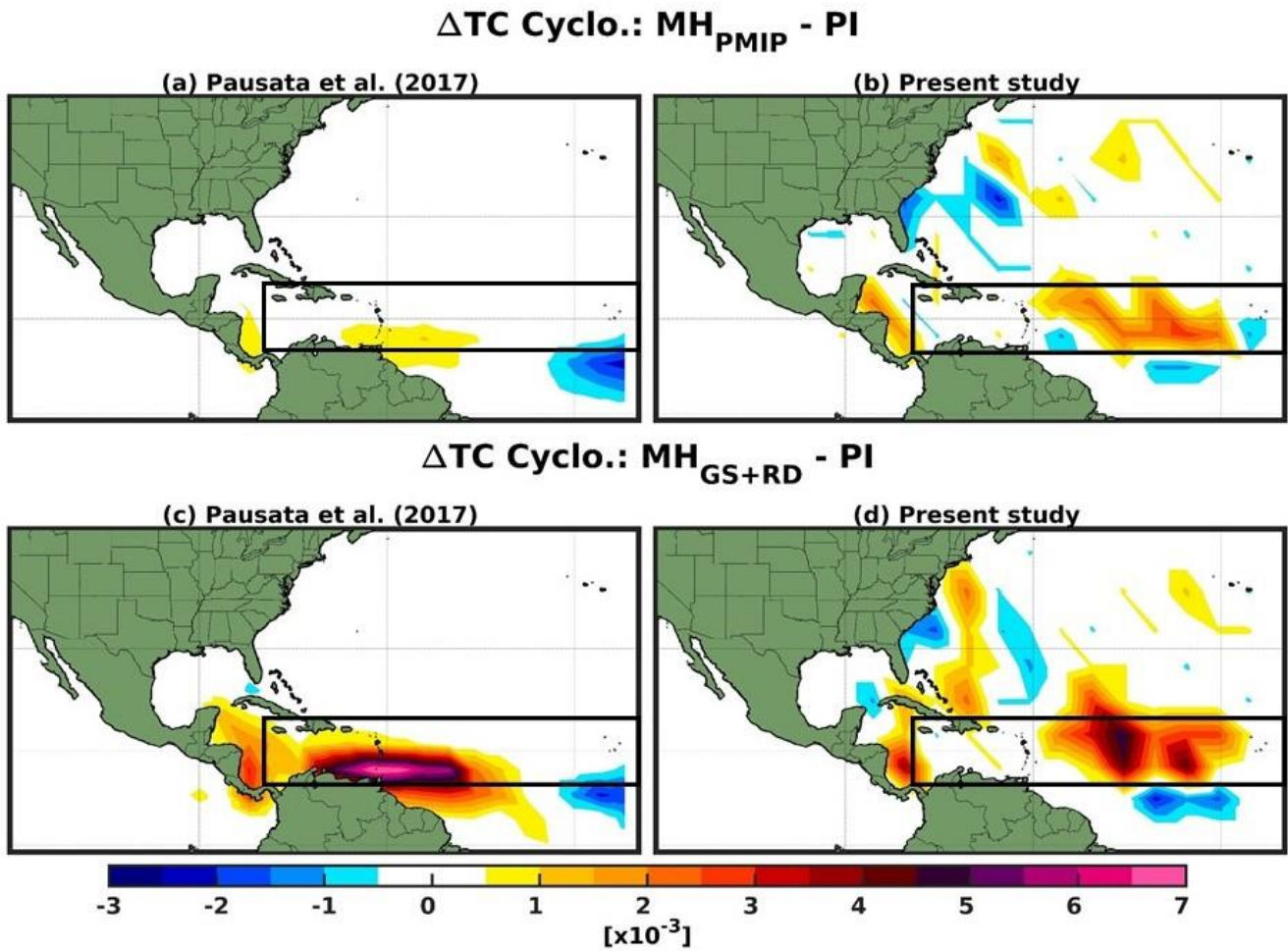
Figure A10: Comparison between TC seasonal cyclogenesis density anomalies for (a – b) MH_PMIP and (c – d) MH_GS+RD relative to PI between (a – c) Pausata et al. (2017) and (b – d) the present study. Note that data are represented over a 5° meshgrid Mercator projection in the present study while in Pausata et al. (2017) a 4° meshgrid is use to represent the fields. The black box shows the approximate present-day main development region (MDR).
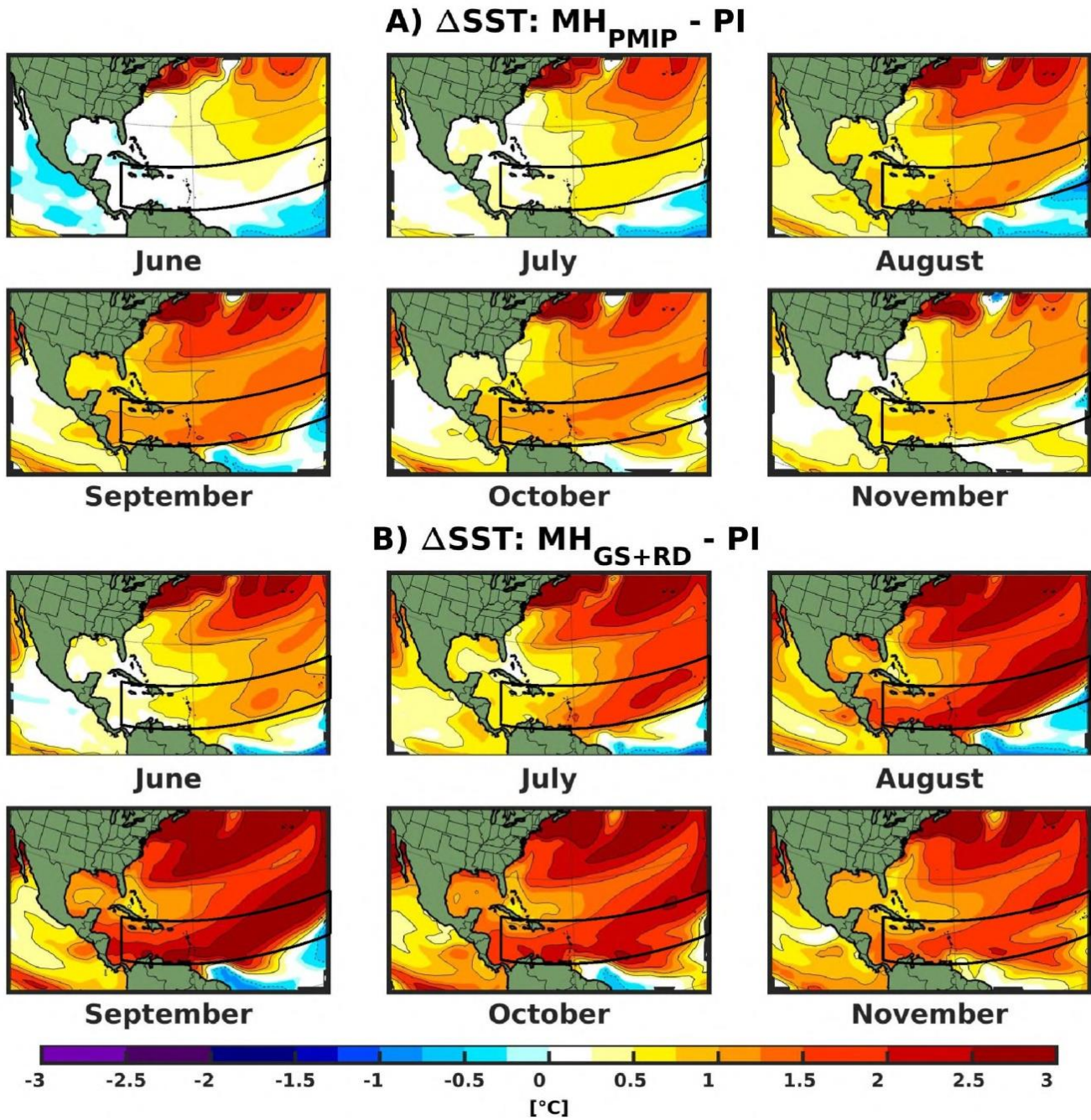
Figure A11: Monthly mean changes in climatological Sea Surface Temperature (SSTs) for (A) MH$_{PMIP}$ and (B) MH$_{GS+RD}$ relative to PI experiment. The black box shows the approximate present-day Main Development Region (MDR). Only values that are significantly different at the 5% level using a local (grid-point) t test are shaded. The contour lines follow the colorbar scale (dashed, negative anomalies; solid, positive anomalies); the 0 line is omitted for clarity.
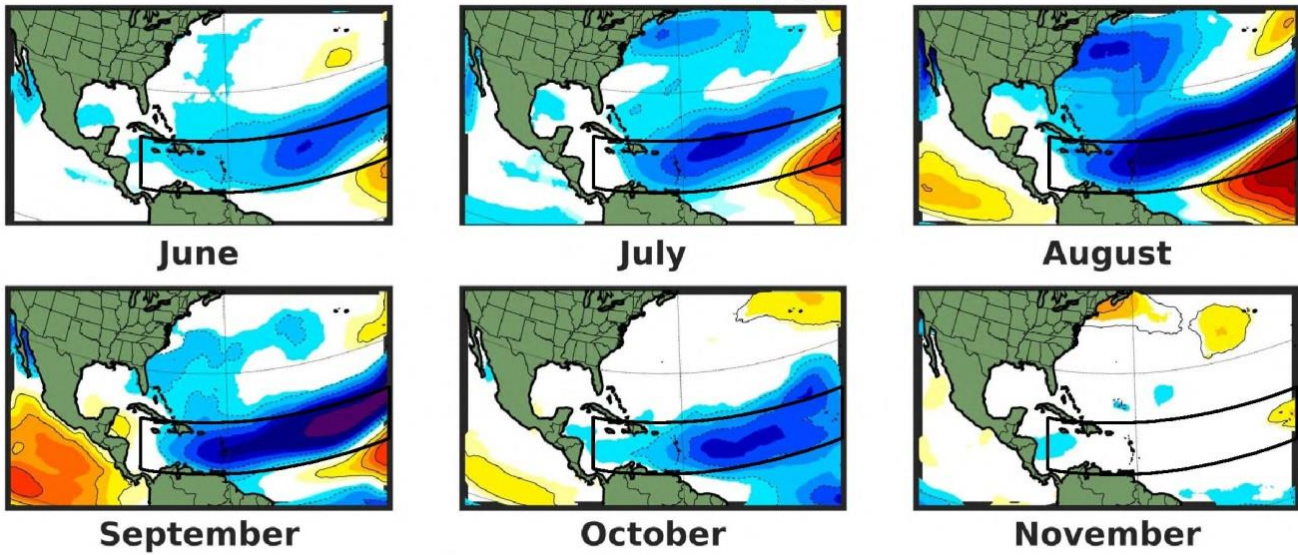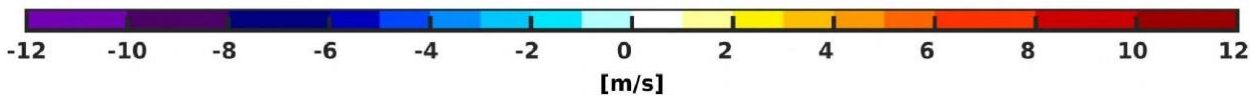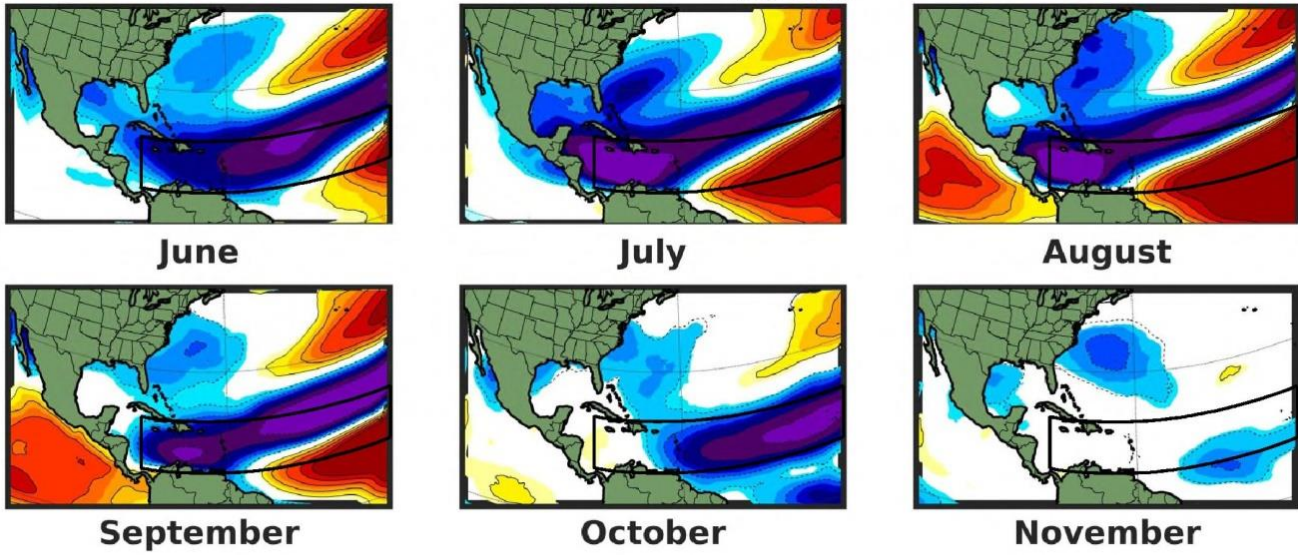
Figure A12: Monthly mean changes in climatological wind shear (200 hPa – 850hPa) for (A) MH_PMIP and (B) MH_GS+RD relative to PI. The black box shows the approximate present-day Main Development Region (MDR). Only values that are significantly different at the 5% level using a local (grid-point) *t* test are shaded. The contour lines follow the colorbar scale (dashed, negative anomalies; solid, positive anomalies); the 0 line is omitted for clarity.
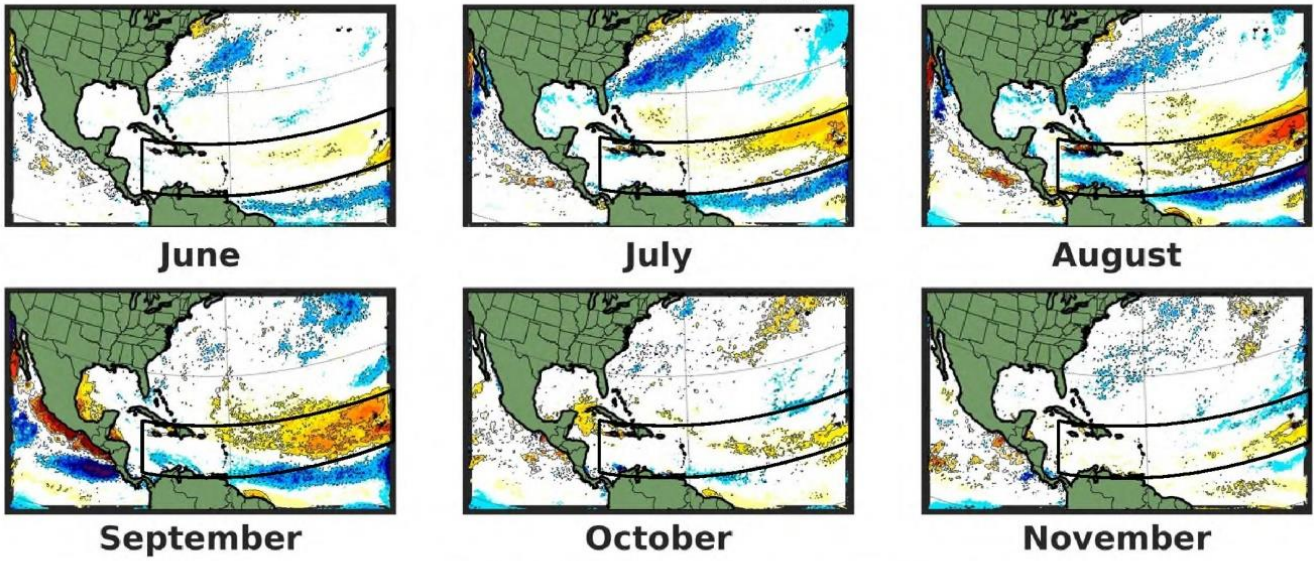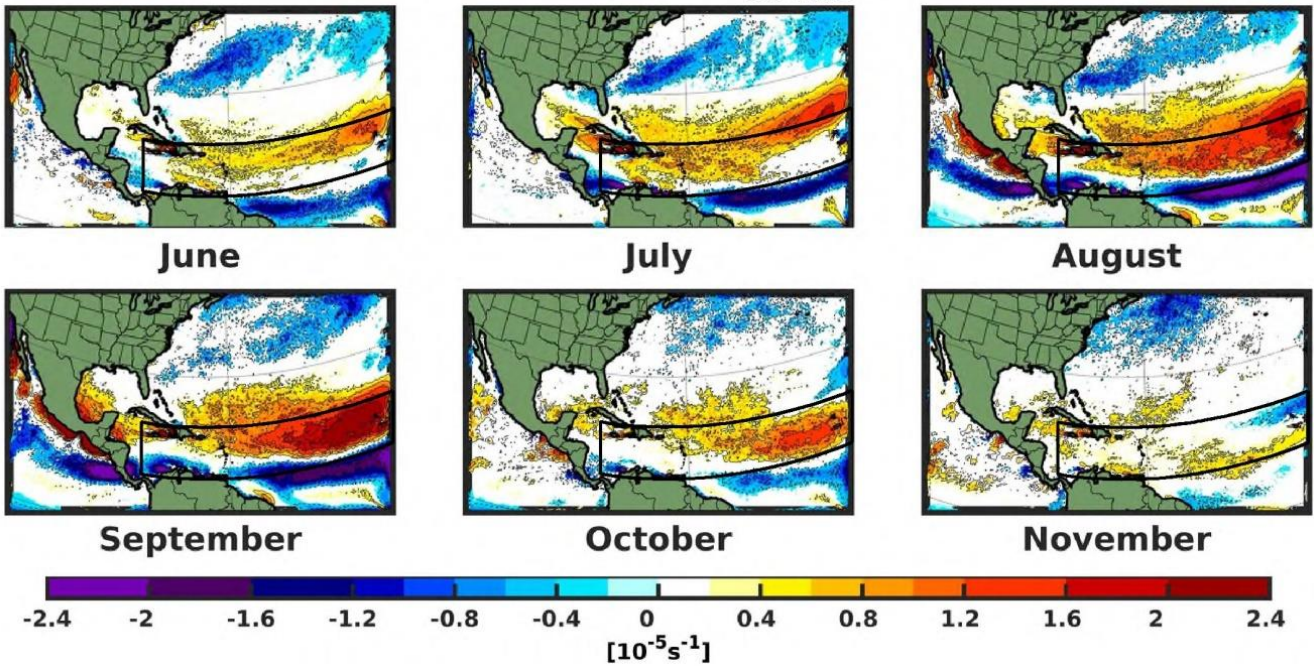
Figure A13: Monthly mean changes in 850 hPa absolute vorticity for (A) MH$_{PMIP}$ and (B) MH$_{GS+RD}$ relative to PI. The black box shows the approximate present-day Main Development Region (MDR). Only values that are significantly different at the 5% level using a local (grid-point) t test are shaded. The contour lines follow the colorbar scale (dashed, negative anomalies; solid, positive anomalies); the 0 line is omitted for clarity.
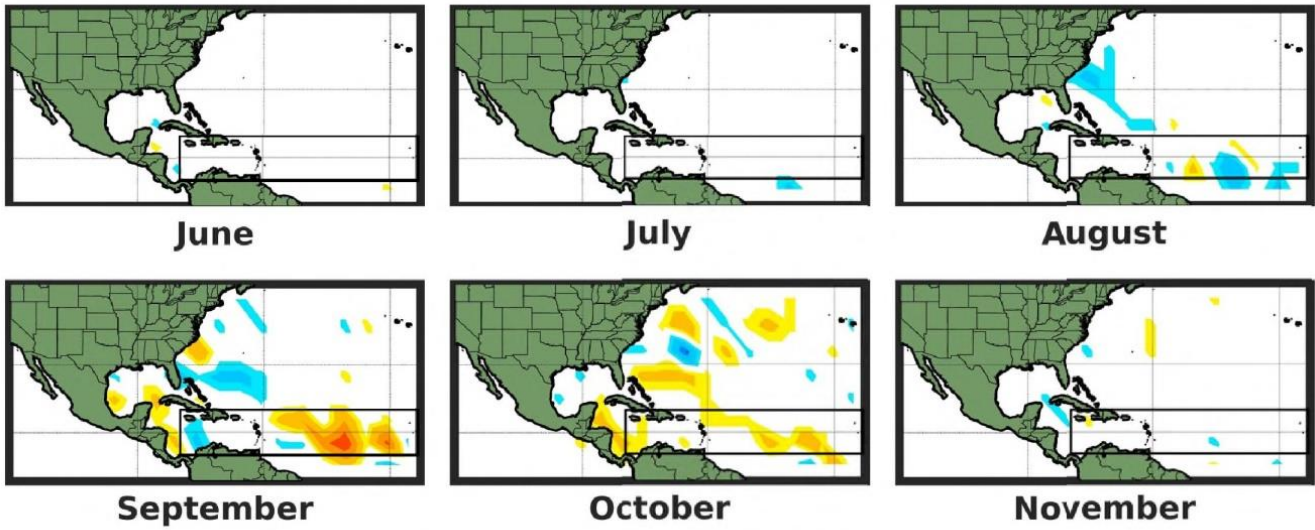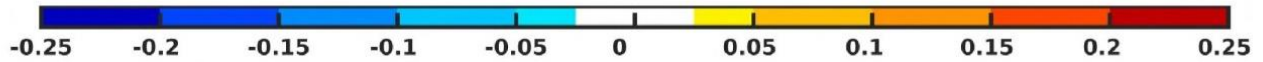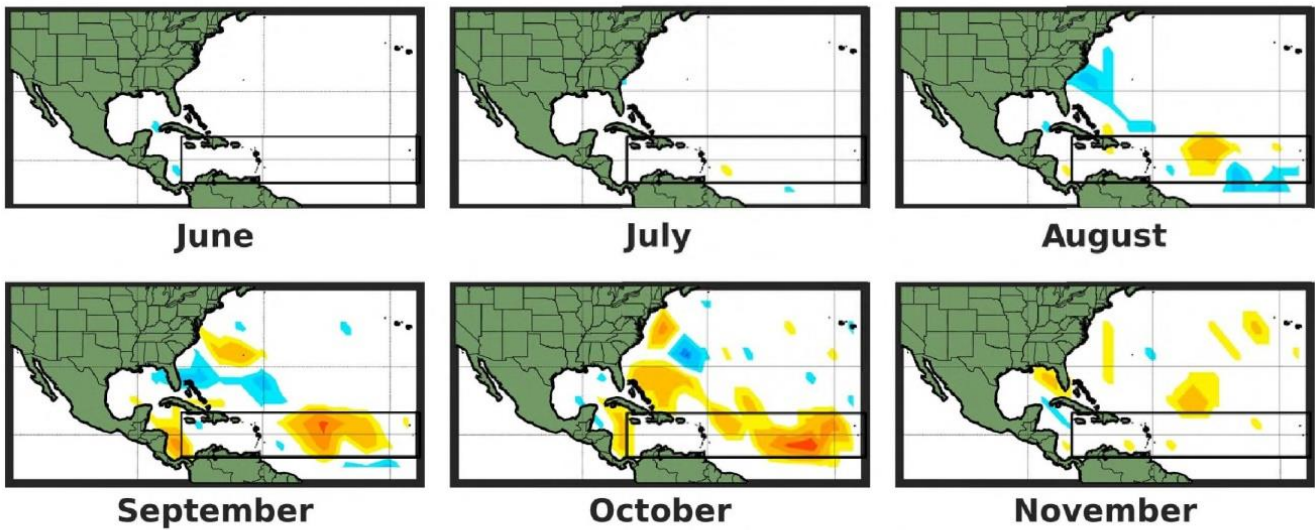
575

Figure A14: TC seasonal (June to November) cyclogenesis density anomaly for (A) MH_{PMIP} and (B) MH_{GS+RD} experiments relative to PI represented over a 5° meshgrid Mercator projection. The black box shows the approximate present-day Main Development Region (MDR).
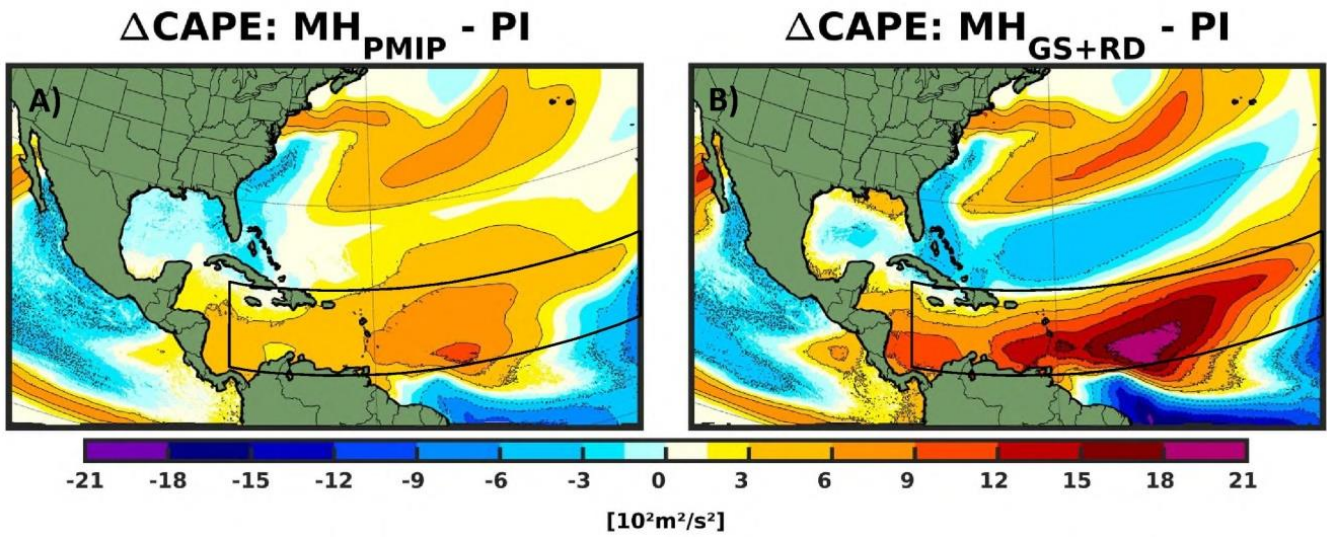
580

Figure A15: Changes in climatological seasonal CAPE between a saturated boundary layer air parcel and an air parcel that has been isothermally lowered to a reference level (June to November, JJASON) for (A) MH_{PMIP} and (B) MH_{GS+RD} experiments relative to PI. The black box shows the approximate present-day main development region (MDR). Only values that are significantly different at the 5% level using a local (grid-point) t test are shaded. The contour lines follow the

585   colorbar scale with different styles (dashed, negative anomalies; solid, positive anomalies); the 0 line is omitted for clarity.

Author contribution

F.S.R.P. conceived the study and designed the experiments with contributions from S.D. and R.L.. K.W. carried out the model simulations and S.D. analyzed the model output. S.D. and K.W. developed the tracking algorithm. S.J.C. and K.E.

590 provided the codes to compute the indexes. All authors contributed to the interpretation of the results. S.D. wrote the manuscript with contributions from all co-authors.

Competing interests

The authors declare that they have no conflict of interest.

Acknowledgments

595 The authors would like to thank Georges Huard and Frédérik Toupin for the technical support, the Recherche en Prévision Numérique (RPN), the Meteorological Research Branch (MRB) and the Canadian Meteorological Centre (CMC) for the permission to use the GEM model as basis for our CRCM6 regional climate model, Qiong Zhang for sharing the global model outputs. This research was enabled in part by support provided by Calcul Québec (https://www.calculquebec.ca/) and Compute Canada (http://www.computecanada.ca). SD, FSRP and RL acknowledge the financial support from the Natural

600 Sciences and Engineering Research Council of Canada (NSERC Grants RGPIN-2018-04981 and RGPIN-2018-04208). FSRP also acknowledge the financial support from the Fond de recherche du Québec - Nature et Technologies (FRQNT Grant 2020-NC-268559).

References

Albani, S., Mahowald, N. M., Perry, A. T., Scanza, R. A., Zender, C. S., Heavens, N. G., ... & Otto-Bliesner, B. L. (2014).

605 Improved dust representation in the Community Atmosphere Model. Journal of Advances in Modeling Earth Systems, 6(3), 541-570.

Albani, S., & Mahowald, N. M. (2019). Paleodust insights into dust impacts on climate. *Journal of Climate*, *32*(22), 7897-7913.

Bélair, S., Mailhot, J., Girard, C., & Vaillancourt, P. (2005). Boundary layer and shallow cumulus clouds in a medium-range

610 forecast of a large-scale weather system. *Monthly Weather Review*, *133*(7), 1938–1960. https://doi.org/10.1175/MWR2958.1

Bell, G.D., M.S. Halpert, R.C. Schnell, R.W. Higgins, J. Lawrimore, V.E. Kousky, R. Tinker, W. Thiaw, M. Chelliah, and A. Artusa, 2000: Climate Assessment for 1999. *Bull. Amer. Meteor. Soc.,* **81**, S1–S50, https://doi.org/10.1175/1520-0477(2000)81[s1:CAF]2.0.CO;2

615   Biasutti, M. (2013). Forced Sahel rainfall trends in the CMIP5 archive. *Journal of Geophysical Research Atmospheres*, *118*(4), 1613–1623. https://doi.org/10.1002/jgrd.50206

Bister, M., & Emanuel, K. A. (1998). Dissipative heating and hurricane intensity. *Meteorology and Atmospheric Physics*, *65*(3–4), 233–240. https://doi.org/10.1007/BF01030791

Bister, M., & Emanuel, K. A. (2002). Low frequency variability of tropical cyclone potential intensity 1. Interannual to
620   interdecadal variability. *Journal of Geophysical Research: Atmospheres*, *107*(D24), ACL-26.

Blender, R., Fraedrich, K., & Lunkeit, F. (1997). Identification of cyclone-track regimes in the North Atlantic. *Quarterly Journal of the Royal Meteorological Society*, *123*(539), 727–741. https://doi.org/10.1256/smsqj.53909

Blender, R., & Schubert, M. (2000). Cyclone tracking in different spatial and temporal resolutions. *Monthly Weather Review*, *128*(2), 377–384. https://doi.org/10.1175/1520-0493(2000)128<0377:CTIDSA>2.0.CO;2

625   Camargo, S. J., Sobel, A. H., Barnston, A. G., & Emanuel, K. A. (2007). Tropical cyclone genesis potential index in climate models. *Tellus, Series A: Dynamic Meteorology and Oceanography*, *59 A*(4), 428–443. https://doi.org/10.1111/j.1600-0870.2007.00238.x

Camargo, S. J., & Wing, A. A. (2016). Tropical cyclones in climate models. *Wiley Interdisciplinary Reviews: Climate Change*, *7*(2), 211-237, doi: 10.1002/wcc.373

630   Caron, L. P., & Jones, C. G. (2012). Understanding and simulating the link between African easterly waves and Atlantic tropical cyclones using a regional climate model: The role of domain size and lateral boundary conditions. *Climate Dynamics*, *39*(1–2), 113–135. https://doi.org/10.1007/s00382-011-1160-8

Copernicus Climate Change Service (C3S). (2017). ERA5: Fifth generation of ECMWF atmospheric reanalyses of the global climate.

635   Donnelly, J. P., & Woodruff, J. D. (2007). Intense hurricane activity over the past 5,000 years controlled by El Niño and the West African monsoon. *Nature*, *447*(7143), 465–468. https://doi.org/10.1038/nature05834

Dunion, J. P., & Velden, C. S. (2004). The impact of the Saharan air layer on Atlantic tropical cyclone activity. Bulletin of the American Meteorological Society, 85(3), 353-366.

Emanuel, K. A. (1995). Sensitivity of Tropical Cyclones to Surface Exchange Coefficients and a Revised Steady-State
640   Model Incorporating Eye Dynamics. *Journal of the Atmospheric Sciences, 52(22)*, 3969-3976).

Emanuel, K. (2006). Climate and tropical cyclone activity: A new model downscaling approach. *Journal of Climate*, *19*(19), 4797-4802.

Emanuel, K. (2010). Tropical cyclone activity downscaled from NOAA-CIRES Reanalysis, 1908–1958. *Journal of Advances in Modeling Earth Systems*, *2*, 12 pp. https://doi.org/10.3894/james.2010.2.1

645   Emanuel, K., Sundararajan, R., & Williams, J. (2008). Hurricanes and Global Warming: Results from Downscaling IPCC AR4 Simulations. *Bulletin of the American Meteorological Society*, *89*(3), 347–368. https://doi.org/10.1175/BAMS-89-3-347

Emanuel, K., & Sobel, A. (2013). Response of tropical sea surface temperature, precipitation, and tropical cyclone-related

variables to changes in global and local forcing. *Journal of Advances in Modeling Earth Systems*, *5*(2), 447-458.

650   Evan, A. T., Dunion, J., Foley, J. A., Heidinger, A. K., & Velden, C. S. (2006). New evidence for a relationship between Atlantic tropical cyclone activity and African dust outbreaks. Geophysical Research Letters, 33(19).

Evan, A. T., Flamant, C., Gaetani, M., & Guichard, F. (2016). The past, present and future of African dust. *Nature*, *531*(7595), 493–495. https://doi.org/10.1038/nature17149

Frank, W. M., & Roundy, P. E. (2006). The Role of Tropical Waves in Tropical Cyclogenesis. *Monthly Weather Review*, 655   *134*(9), 2397–2417. https://doi.org/10.1175/mwr3204.1

Gaetani, M., Messori, G., Zhang, Q., Flamant, C., & Pausata, F. S. R. (2017). Understanding the mechanisms behind the northward extension of the West African monsoon during the mid-holocene. *Journal of Climate*, *30*(19), 7621–7642. https://doi.org/10.1175/JCLI-D-16-0299.1

Giannini, A., & Kaplan, A. (2019). The role of aerosols and greenhouse gases in Sahel drought and recovery. *Climatic* 660   *Change*, *152*(3–4), 449–466. https://doi.org/10.1007/s10584-018-2341-9

Girard, C., Plante, A., Desgagné, M., Mctaggart-Cowan, R., Côté, J., Charron, M., … Zadra, A. (2014). Staggered vertical discretization of the canadian environmental multiscale (GEM) model using a coordinate of the log-hydrostatic-pressure type. *Monthly Weather Review*, *142*(3), 1183–1196. https://doi.org/10.1175/MWR-D-13-00255.1

Gray, W. M. (1975). Tropical Cyclone Genesis. *Dept. of Atmos. Sci. Colarado State University, Fort Collins, CO, 121.*, 665   *Paper No.* 120.

Gray, W. M. (1979). Hurricanes: Their formation, structure and likely role in the tropical circulation. *Meteorology Over Tropical Oceans*, 155–218. Retrieved from http://ci.nii.ac.jp/naid/10006708334/en/

Greer, L., & Swart, P. K. (2006). Decadal cyclicity of regional mid-Holocene precipitation: Evidence from Dominican coral proxies. *Paleoceanography*, *21*(2), 1–17. https://doi.org/10.1029/2005PA001166

670   Gualdi, S., Scoccimarro, E., & Navarra, A. (2008). Changes in tropical cyclone activity due to global warming: Results from a high-resolution coupled general circulation model. *Journal of Climate*, *21*(20), 5204–5228. https://doi.org/10.1175/2008JCLI1921.1

Hazeleger, W., Wang, X., Severijns, C., Ştefănescu, S., Bintanja, R., Sterl, A., … van der Wiel, K. (2012). EC-Earth V2.2: Description and validation of a new seamless earth system prediction model. *Climate Dynamics*, *39*(11), 2611–2629. 675   https://doi.org/10.1007/s00382-011-1228-5

Hess, M., Koepke, P., & Schult, I. (1998). Optical properties of aerosols and clouds: The software package OPAC. *Bulletin of the American meteorological society*, *79*(5), 831-844.

Hodges, K., Cobb, A., & Vidale, P.L, (2017). How well are tropical cyclones represented in reanalysis datasets? *Journal of Climate*, 30, 5243–5264, doi: 10.1175/JCLI-D-16-0557.1

680   Holmes, J. A. (2008). Ecology. How the Sahara became dry. *Science (New York, N.Y.)*, *320*(5877), 752–753. https://doi.org/10.1126/science.1158105

Hopcroft, P. O., & Valdes, P. J. (2019). On the role of dust-climate feedbacks during the mid-Holocene. *Geophysical*

Research Letters, *46*(3), 1612-1621.

Joussaume, S., Taylor, K. E., Mitchell, F. B., Kutzbach, E., Harrison, S. P., Prentice, I. C., … Wyputta, U. (1999). *Monsoon changes for 6000 years ago results of 18 simulations from the Paleoclimate modeling intercomparison project.pdf*. *26*(7), 859–862.

Kain, J. S., & Fritsch, J. M. (1990). A One-Dimensional Entertaining/Detraining Plume Model and Its Application in Convective Parametrization. *Journal of the Atmospheric Sciences*, 47(23), 2784-2280.

Kim, D., Moon, Y., Camargo, S. J., Wing, A. A., Sobel, A. H., Murakami, H., ... & Page, E. (2018). Process-oriented diagnosis of tropical cyclones in high-resolution GCMs. *Journal of Climate*, *31*(5), 1685-1702.

Knutson, T., Camargo, S. J., Chan, J. C. L., Emanuel, K., Ho, C.-H., Kossin, J., … Wu, L. (2020). Tropical Cyclones and Climate Change Assessment: Part II. Projected Response to Anthropogenic Warming. *Bulletin of the American Meteorological Society*, 1–62. https://doi.org/10.1175/bams-d-18-0194.1

Knutson, T. R., Sirutis, J. J., Vecchi, G. A., Garner, S., Zhao, M., Kim, H. S., … Villarini, G. (2013). Dynamical downscaling projections of twenty-first-century atlantic hurricane activity: CMIP3 and CMIP5 model-based scenarios. *Journal of Climate*, *26*(17), 6591–6617. https://doi.org/10.1175/JCLI-D-12-00539.1

Koh, J. H., & Brierley, C. M. (2015). Tropical cyclone genesis across palaeoclimates. *Climate of the Past Discussions*, *11*(1), 181–220. https://doi.org/10.5194/cp-11-1433-2015

Korty, R. L., Camargo, S. J., & Galewsky, J. (2012). Variations in tropical cyclone genesis factors in simulations of the Holocene epoch. *Journal of Climate*, *25*(23), 8196–8211. https://doi.org/10.1175/JCLI-D-12-00033.1

Kowalski, K., Neer, W. van, Bocheński, Z., Młynarski, M., Rzebik-Kowalska, B., Szyndlar, Z., … Wendorf, F. (1989). A last interglacial fauna from the Eastern Sahara. *Quaternary Research*, *32*(3), 335–341. https://doi.org/10.1016/0033-5894(89)90099-9

Kuo, H. L. (1965). On Formation and Intensification of Tropical Cyclones Through Latent Heat Release by Cumulus Convection. *Journal of the Atmospheric Sciences*, 22, 40-63.

Landman, W. A., Seth, A., & Camargo, S. J. (2005). The effect of regional climate model domain choice on the simulation of tropical cyclone-like vortices in the southwestern Indian Ocean. *Journal of Climate*, *18*(8), 1263–1274. https://doi.org/10.1175/JCLI3324.1

Landsea, C. (2014). FAQ E17) How many hurricanes have there been in each month? Retrieved August 29, 2019, from aoml.noaa.gov website: https://www.aoml.noaa.gov/hrd/tcfaq/E17.html

Landsea, C. W., & Franklin, J. L. (2013). Atlantic hurricane database uncertainty and presentation of a new database format. *Monthly Weather Review*, *141*(10), 3576–3592. https://doi.org/10.1175/MWR-D-12-00254.1

Landsea, C. W. (1993). A Climatology of Intense (or Major) Atlantic Hurricanes. *Monthly Weather Review*, *121*(6), 1703–1713.

Lau, K. M., Kim, K. M., Sud, Y. C., & Walker, G. K. (2009). A GCM study of the response of the atmospheric water cycle of West Africa and the Atlantic to Saharan dust radiative forcing. In *Annales Geophysicae* (Vol. 27, No. 10, pp. 4023-

4037). Copernicus GmbH.

Liu, K. B., & Fearn, M. L. (2000). Reconstruction of prehistoric landfall frequencies of catastrophic hurricanes in Northwestern Florida from lake sediment records. *Quaternary Research*, *54*(2), 238–245. https://doi.org/10.1006/qres.2000.2166

Martynov, A., Sushama, L., Laprise, R., Winger, K., & Dugas, B. (2012). Interactive lakes in the Canadian Regional Climate Model, version 5: the role of lakes in the regional climate of North America. *Tellus A: Dynamic Meteorology and Oceanography*, *64*(1), 16226.

McTaggart-Cowan, R., Vaillancourt, P. A., Zadra, A., Chamberland, S., Charron, M., Corvec, S., ... & Separovic, L. (2019). Modernization of atmospheric physics parameterization in Canadian NWP. *Journal of Advances in Modeling Earth Systems*, *11*(11), 3593-3635.

Merlis, T. M., Zhao, M., & Held, I. M. (2013). The sensitivity of hurricane frequency to ITCZ changes and radiatively forced warming in aquaplanet simulations. *Geophysical Research Letters*, *40*(15), 4109–4114. https://doi.org/10.1002/grl.50680

Mironov, D. V. (2008). Parametrization of Lakes in Numerical Weather Prediction: Description of a Lake Model. Physical Review Letter, 91, (pp. 41-pp). DWD. https://doi.org/10.1103/PhysRevLett.91.139903

Murakami, H., 2014: Tropical cyclones in reanalysis data sets. *Geophysical Research Letters*, 41, 2133-2141, doi: 10.1002/2014GL059519.

Murray, R. J., & Simmonds, I. (1991). A numerical scheme for tracking cyclone centres from digital data. Part II: Application to January and July general circulation model simulations. *Australian Meteorological Magazine*, 39, 167–180.

Patricola, C. M., Saravanan, R., & Chang, P. (2018). The Response of Atlantic Tropical Cyclones to Suppression of African Easterly Waves. *Geophysical Research Letters*, *45*(1), 471–479. https://doi.org/10.1002/2017GL076081

Pausata, F. S. R., Emanuel, K. A., Chiacchio, M., Diro, G. T., Zhang, Q., Sushama, L., … Donnelly, J. P. (2017). Tropical cyclone activity enhanced by Sahara greening and reduced dust emissions during the African Humid Period. *Proceedings of the National Academy of Sciences*, *114*(24), 6221–6226. https://doi.org/10.1073/pnas.1619111114

Pausata, F. S. R., Messori, G., & Zhang, Q. (2016). Impacts of dust reduction on the northward expansion of the African monsoon during the Green Sahara period. *Earth and Planetary Science Letters*, *434*, 298–307. https://doi.org/10.1016/j.epsl.2015.11.049

Reed, K. A., Bacmeister, J. T., Huff, J. J. A., Wu, X., Bates, S. C., & Rosenbloom, N. A. (2019). Exploring the Impact of Dust on North Atlantic Hurricanes in a High-Resolution Climate Model. *Geophysical Research Letters*, *46*(2), 1105–1112. https://doi.org/10.1029/2018GL080642

Rohling, E. ., Sprovieri, M., Cane, T., Casford, J. S. ., Cooke, S., Bouloubassi, I., … Kroon, D. (2004). Reconstructing past planktic foraminiferal habitats using stable isotope data: a case history for Mediterranean sapropel S5. *Marine Micropaleontology*, *50*(1–2), 89–123. https://doi.org/10.1016/S0377-8398(03)00068-9

Russell, J. O., Aiyyer, A., White, J. D., & Hannah, W. (2017). Revisiting the connection between African Easterly Waves and Atlantic tropical cyclogenesis. *Geophysical Research Letters*, *44*(1), 587–595. https://doi.org/10.1002/2016GL071236

Schneider, T., Bischoff, T., & Haug, G. H. (2014). Migrations and dynamics of the intertropical convergence zone. *Nature*, *513*(7516), 45–53. https://doi.org/10.1038/nature13636

Schubert, M., Perlwitz, J., Blender, R., Fraedrich, K., & Lunkeit, F. (1998). North Atlantic cyclones in CO2-induced warm climate simulations: Frequency, intensity, and tracks. *Climate Dynamics*, *14*(11), 827–837. https://doi.org/10.1007/s003820050258

Scoccimarro, E., Fogli, P. G., Reed, K. A., Gualdi, S., Masina, S., & Navarra, A. (2017). Tropical cyclone interaction with the ocean: The role of high-frequency (subdaily) coupled processes. *Journal of Climate*, *30*(1), 145–162. https://doi.org/10.1175/JCLI-D-16-0292.1

Scoccimarro, E., Gualdi, S., Bellucci, A., Sanna, A., Fogli, P. G., Manzini, E., … Navarra, A. (2011). Effects of tropical cyclones on ocean heat transport in a high-resolution coupled general circulation model. *Journal of Climate*, *24*(16), 4368–4384. https://doi.org/10.1175/2011JCLI4104.1

Seth, A., Giannini, A., Rojas, M., Rauscher, S. A., Bordoni, S., Singh, D., & Camargo, S. J. (2019). Monsoon responses to climate changes—connecting past, present and future. *Current Climate Change Reports*, *5*(2), 63-79.

Shaevitz, D. A., Camargo, S. J., Sobel, A. H., Jonas, J. A., Kim, D., Kumar, A., … Henderson, N. (2014). Characteristics of tropical cyclones in high-resolution models in the present climate. *Journal of Advances in Modeling Earth Systems*, *6*(4), 1154–1172. https://doi.org/doi:10.1002/2014MS000372

Shanahan, T. M., Overpeck, J. T., Anchukaitis, K. J., Beck, J. W., Cole, J. E., Dettman, D. L., … King, J. W. (2009). Atlantic forcing of persistent drought in West Africa. *Science*, *324*(5925), 377–380. https://doi.org/10.1126/science.1166352

Sinclair, M. R. (1997). Objective identification of cyclones and their circulation intensity, and climatology. *Weather and Forecasting*, *12*(3 PART II), 595–612.

Solmon, F., Mallet, M., Elguindi, N., Giorgi, F., Zakey, A., & Konaré, A. (2008). Dust aerosol impact on regional precipitation over western Africa, mechanisms and sensitivity to absorption properties. *Geophysical Research Letters*, *35*(24).

Strachan, J., Vidale, P. L., Hodges, K., Roberts, M., & Demory, M. E. (2013). Investigating global tropical cyclone activity with a hierarchy of AGCMs: The role of model resolution. *Journal of Climate*, *26*(1), 133–152. https://doi.org/10.1175/JCLI-D-12-00012.1

Taylor, K. E., Stouffer, R. J., & Meehl, G. A. (2012). An overview of CMIP5 and the experiment design. *Bulletin of the American Meteorological Society*, *93*(4), 485–498. https://doi.org/10.1175/BAMS-D-11-00094.1

Thompson, A. J., Skinner, C. B., Poulsen, C. J., & Zhu, J. (2019). Modulation of mid-Holocene African rainfall by dust aerosol direct and indirect effects. *Geophysical Research Letters*, *46*(7), 3917-3926.

785   Thorncroft, C., & Hodges, K. (2001). African easterly wave variability and its relationship to Atlantic tropical cyclone activity. *Journal of Climate*, *14*(6), 1166–1179. https://doi.org/10.1175/1520-0442(2001)014<1166:AEWVAI>2.0.CO;2

Tippett, M. K., Camargo, S. J., & Sobel, A. H. (2011). A poisson regression index for tropical cyclone genesis and the role of large-scale vorticity in genesis. *Journal of Climate*, *24*(9), 2335–2357. https://doi.org/10.1175/2010JCLI3811.1

790   Toomey, M. R., Curry, W. B., Donnelly, J. P., & Van Hengstum, P. J. (2013). Reconstructing 7000 years of North Atlantic hurricane variability using deep-sea sediment cores from the western Great Bahama Bank. *Paleoceanography*, *28*(1), 31–41. https://doi.org/10.1002/palo.20012

Vecchi, G. A., Delworth, T. L., Murakami, H., Underwood, S. D., Wittenberg, A. T., Zeng, F., ... & He, J. (2019). Tropical cyclone sensitivities to CO_2 doubling: roles of atmospheric resolution, synoptic variability and background climate

795   changes. *Climate Dynamics*, *53*(9-10), 5999-6033, doi: 10.1007/s00382-019-04913-y

Verseghy, D. L. (2000). The Canadian land surface scheme (CLASS): Its history and future. *Atmosphere - Ocean*, *38*(1), 1–13. https://doi.org/10.1080/07055900.2000.9649637

Verseghy, D. (2009). *CLASS–The Canadian Land Surface Scheme (Version 3.4), Technical Documentation (Version 1.1)*. (January), 180. http://www.usask.ca/ip3/download/CLASS_v3_4_Documentation_v1_1.pdf

800   Walsh, K. (1997). Objective detection of tropical cyclones in high-resolution analyses. *Monthly Weather Review*, *125*(8), 1767–1779. https://doi.org/10.1175/1520-0493(1997)125<1767:ODOTCI>2.0.CO;2

Walsh, K. J. E., Fiorino, M., Landsea, C. W., & McInnes, K. L. (2007). Objectively determined resolution-dependent threshold criteria for the detection of tropical cyclones in climate models and reanalyses. *Journal of Climate*, *20*(10), 2307–2314. https://doi.org/10.1175/JCLI4074.1

805   Walsh, K., Lavender, S., Scoccimarro, E., & Murakami, H. (2013). Resolution dependence of tropical cyclone formation in CMIP3 and finer resolution models. *Climate Dynamics*, *40*(3–4), 585–599. https://doi.org/10.1007/s00382-012-1298-z

Walsh, K. J. E., Mcbride, J. L., Klotzbach, P. J., Balachandran, S., Camargo, S. J., Holland, G., … Sugi, M. (2016). Tropical cyclones and climate change. *Wiley Interdisciplinary Reviews: Climate Change*, *7*(1), 65–89. https://doi.org/10.1002/wcc.371

810   Wing, A. A., Camargo, S. J., Sobel, A. H., Kim, D., Moon, Y., Murakami, H., … Zhao, M. (2019). Moist Static Energy Budget Analysis of Tropical Cyclone Intensification in High-Resolution Climate Models. *Journal of Climate*, *32*(18), 6071–6095. https://doi.org/10.1175/JCLI-D-18-0599.1

Zarzycki, C. M., & Ullrich, P. A. (2017). Assessing sensitivities in algorithmic detection of tropical cyclones in climate data. *Geophysical Research Letters*, *44*(2), 1141–1149. https://doi.org/10.1002/2016GL071606

815

Simulation	Orbital forcing	GHGs	Saharan vegetation	Saharan dust
PI	1950 AD	1850 AD	Desert	PI
MH$_{PMIP}$	6,000 yBP	6,000 yBP	As PI	As PI
MH$_{GS+RD}$	6,000 yBP	6,000 yBP	Shrub	Reduced

Table 1: Boundary conditions for each modeling experiment.
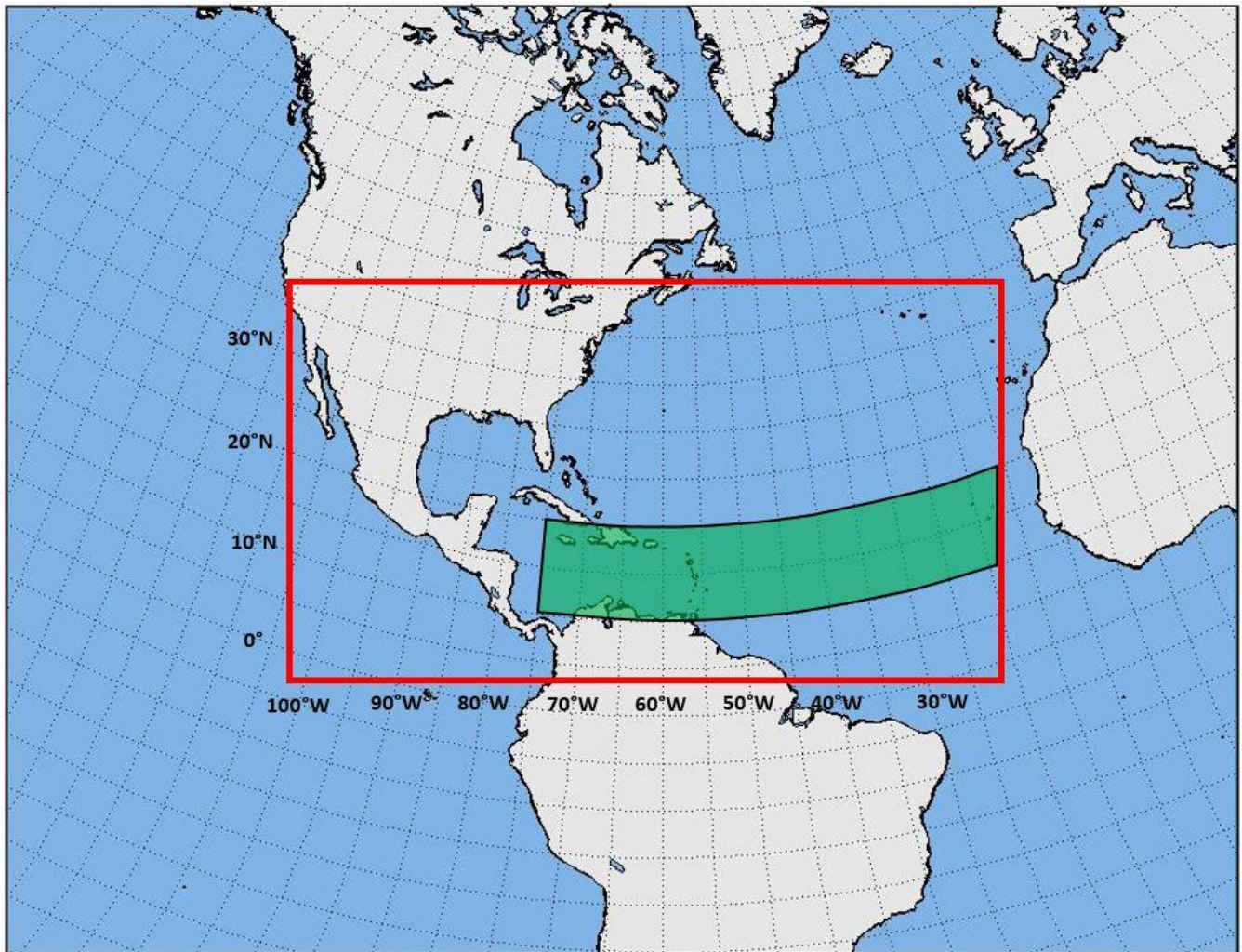
Figure 1: CRCM6 simulation domain (red box). The black/green shaded box shows the approximate present-day Tropical Cyclones Main Development Region (MDR). Note that the data are projected over an Equidistant Cylindrical Projection.
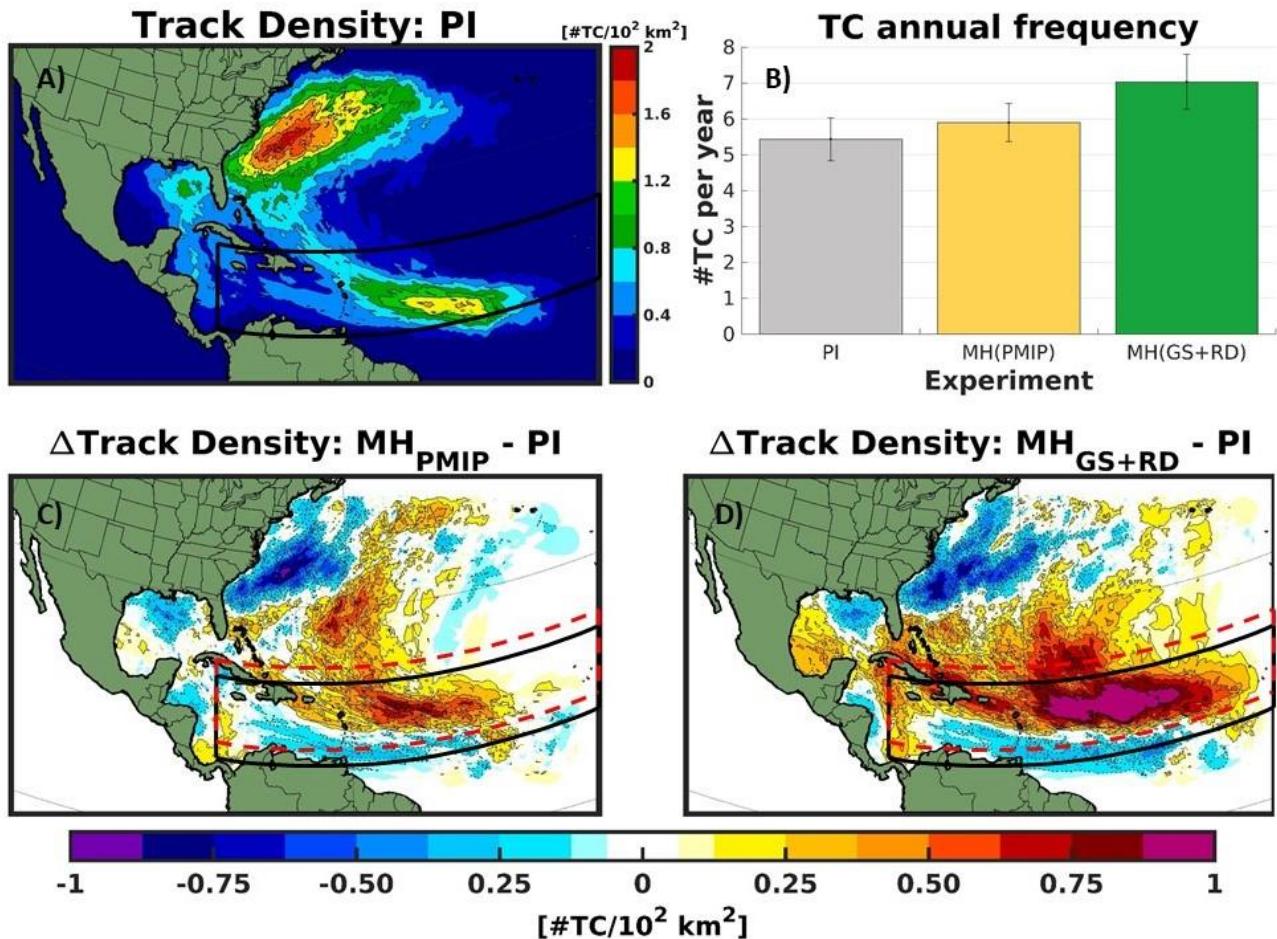
Figure 2: June to November (JJASON) climatology of (A) track density for the preindustrial experiment (PI); (B) TC frequency in the Atlantic Ocean for each experiment. Error bars (whiskers) indicate the standard error of the mean; Changes in track density for the MH$_{PMIP}$ (C) and the MH$_{GS+RD}$ (D) experiments relative to the PI. The black box shows the present-day main development region (MDR), the red dotted box shows the approximate shift of the MDR in the MH experiments. Only values that are significantly different at the 5% level using a local (grid-point) *t* test are shaded. The contour lines follow the colorbar scale (dashed, negative anomalies; solid, positive anomalies); the 0 line is omitted for clarity.
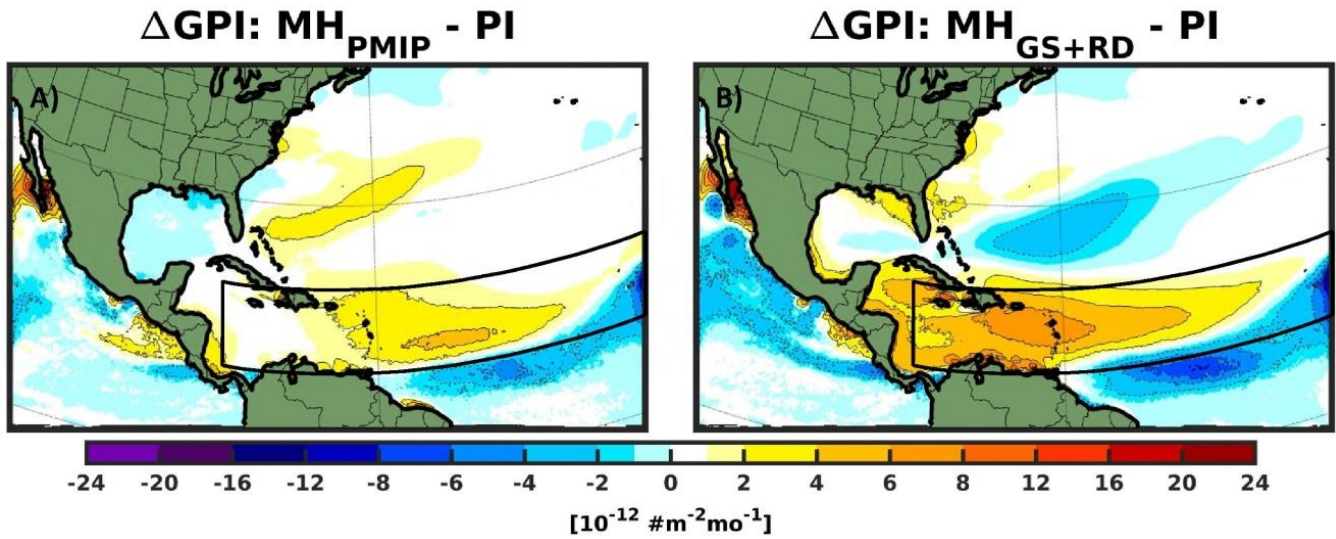
Figure 3: Changes in seasonal Genesis Potential Index - GPI (June to November, JJASON) for (A) MH_{PMIP} and (B) MH_{GS+RD} experiments relative to PI. The black box shows the approximate present-day main development region (MDR). Only values that are significantly different at the 5% level using a local (grid-point) t test are shaded. The contour lines follow the colorbar scale (dashed, negative anomalies; solid, positive anomalies); the 0 line is omitted for clarity.
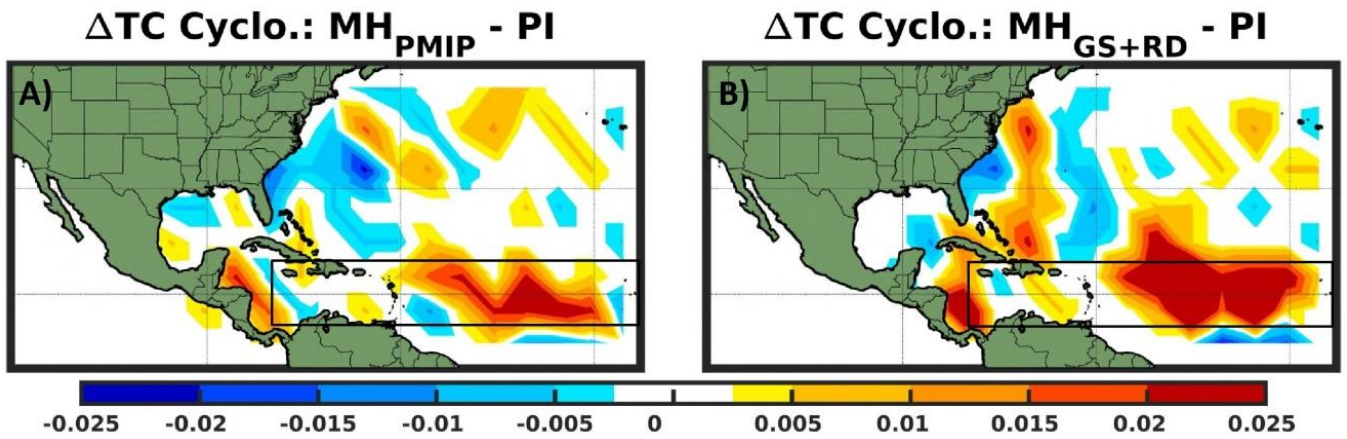
845

Figure 4: TC seasonal (June to November) cyclogenesis density anomaly for (A) MH_{PMIP} and (B) MH_{GS+RD} experiments relative to PI represented over a 5° meshgrid Mercator projection. The black box shows the approximate present-day main development region (MDR).
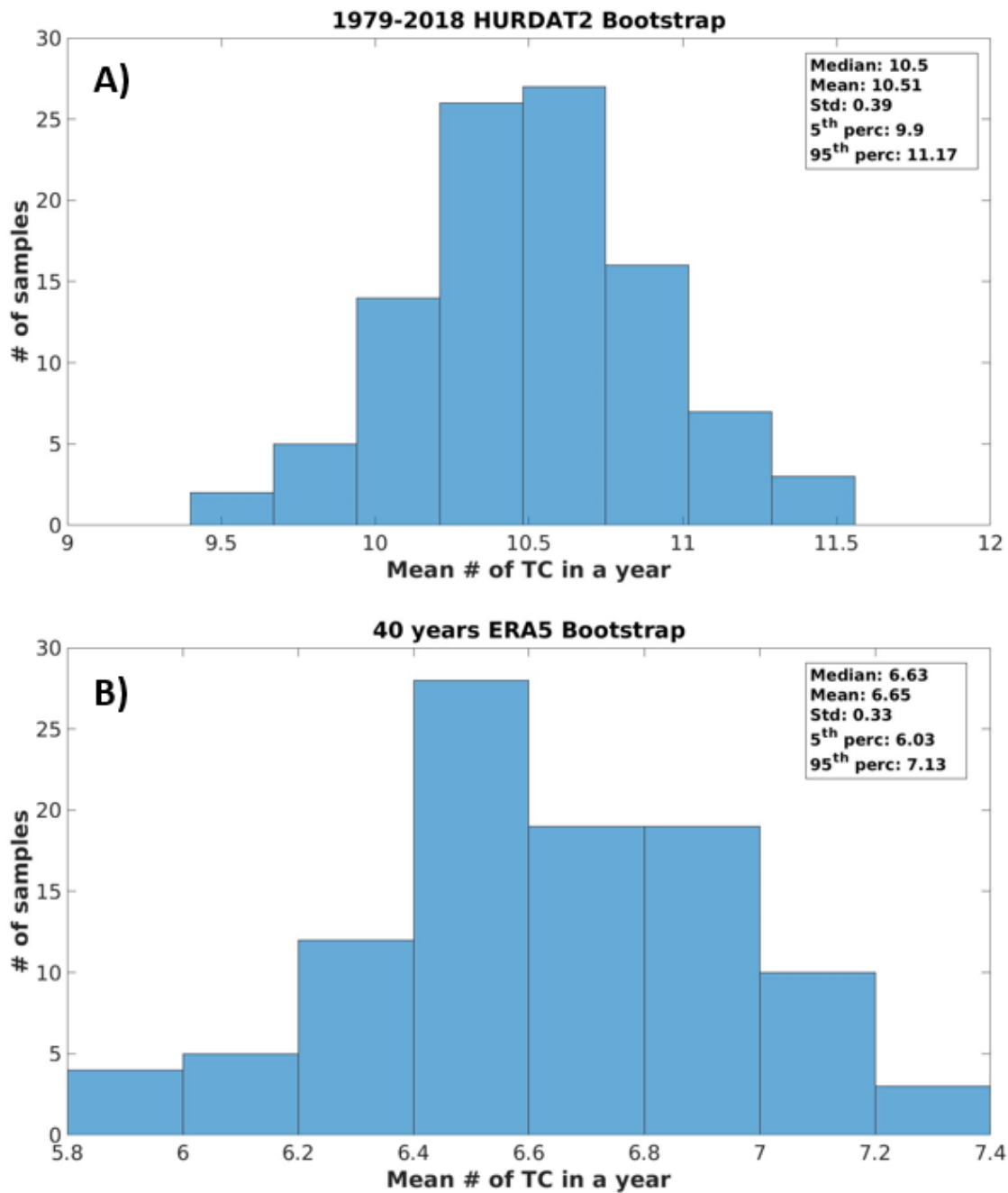
850

Figure 5: Bootstrap distributions based on (A) 1979-2018 HURDAT database and (B) 1979-2018 ERA5 reanalysis data. Legend presents the median, mean, standard deviation, 5th and 95th percentiles of the distributions.
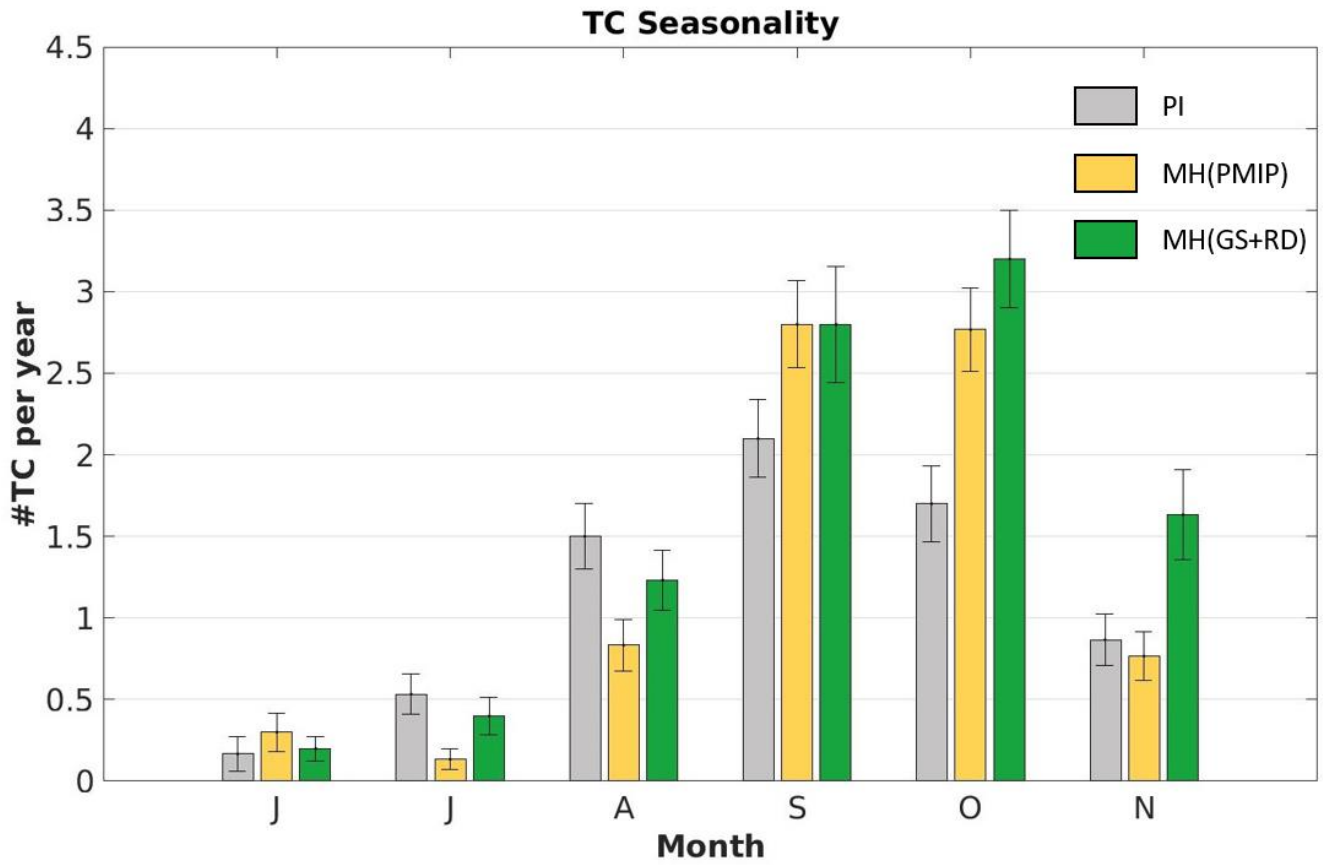
855   **Figure 6:** TC climatological distribution throughout the extended TC season (June to November) for each experiment. Error bars (whiskers) indicate the standard error of the mean.
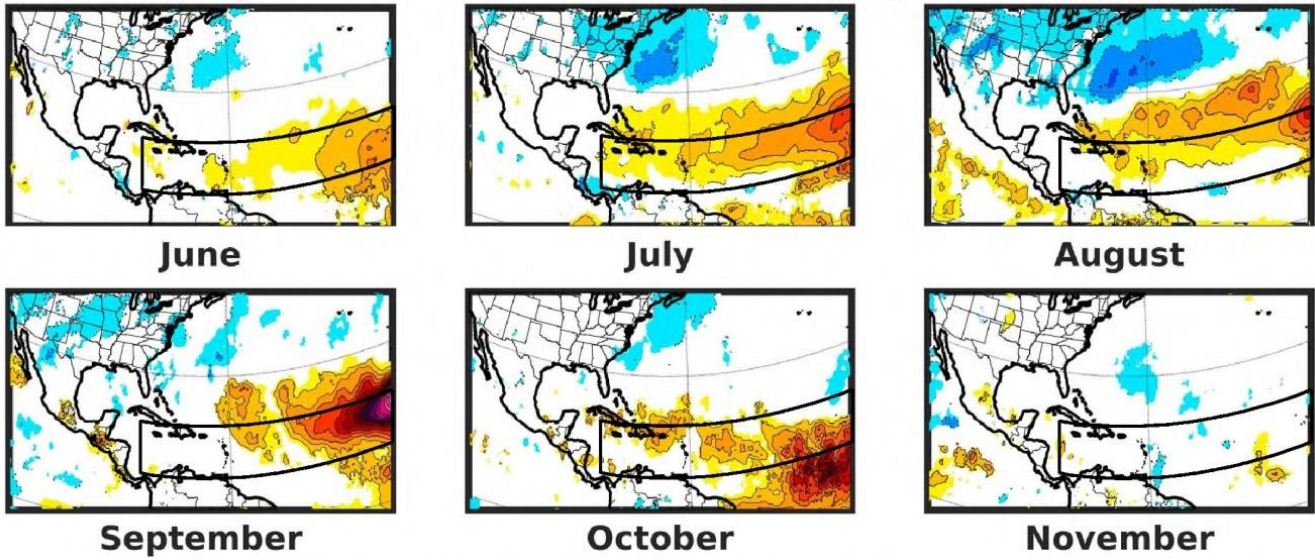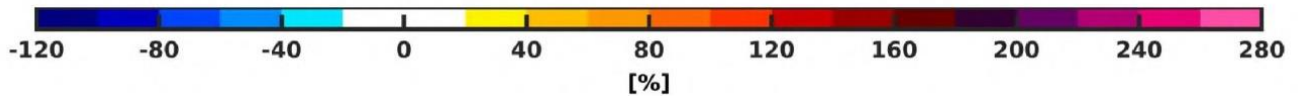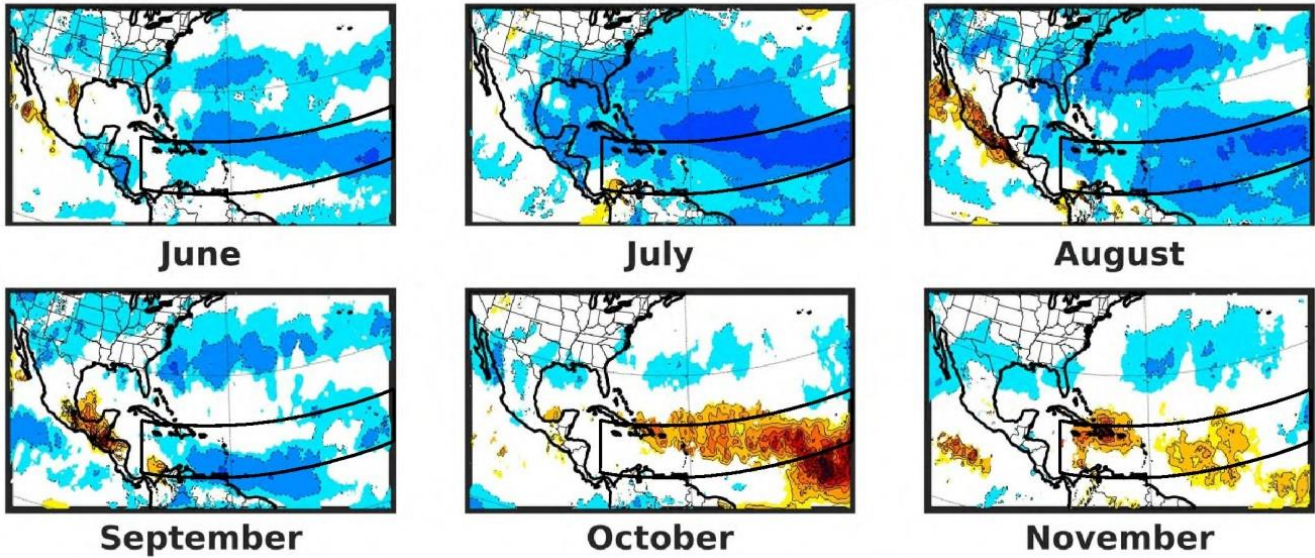
Figure 7: Monthly African Easterly Waves (AEWs) anomalies represented through the variance of the meridional wind at 700 hPa, filtered in the 2.5- to 5-day band, for (A) MH$_{PMIP}$ and (B) MH$_{GS+RD}$ relative to PI. The black box shows the approximate present-day main development region (MDR). Only values that are significantly different at the 5% level using a local (grid-point) t test are shaded. The contour lines follow the colorbar scale (dashed, negative anomalies; solid, positive anomalies); the 0 line is omitted for clarity.
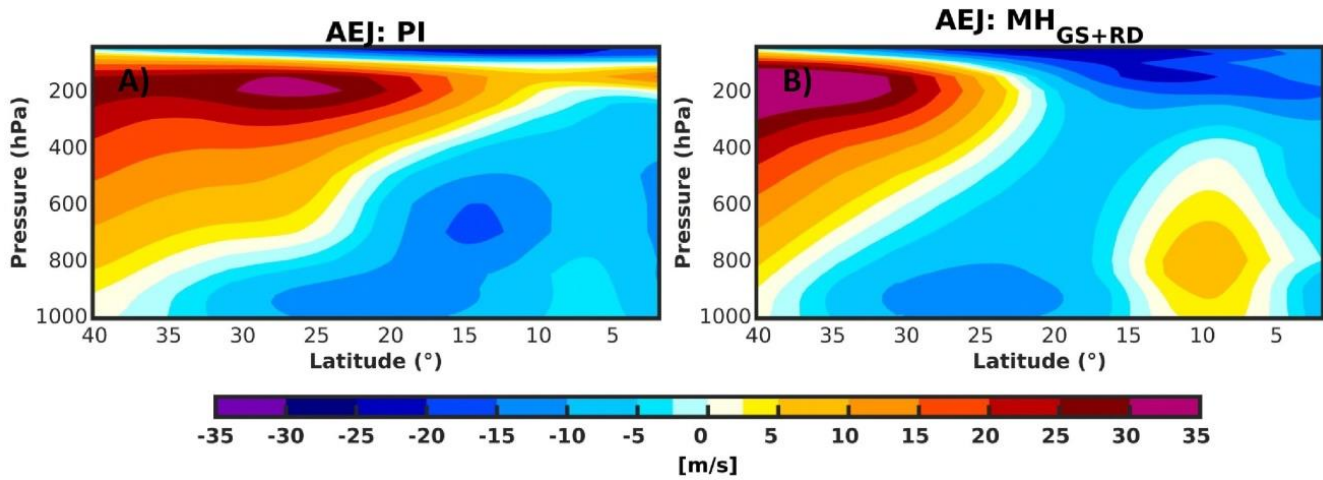
865   **Figure 8:** African Easterly Jet (AEJ) represented through a vertical cross section of zonal mean (0-40°N; 20°W-30°W) seasonal climatological zonal winds for (A) PI and (B) MH$_{GS+RD}$ experiments, respectively.
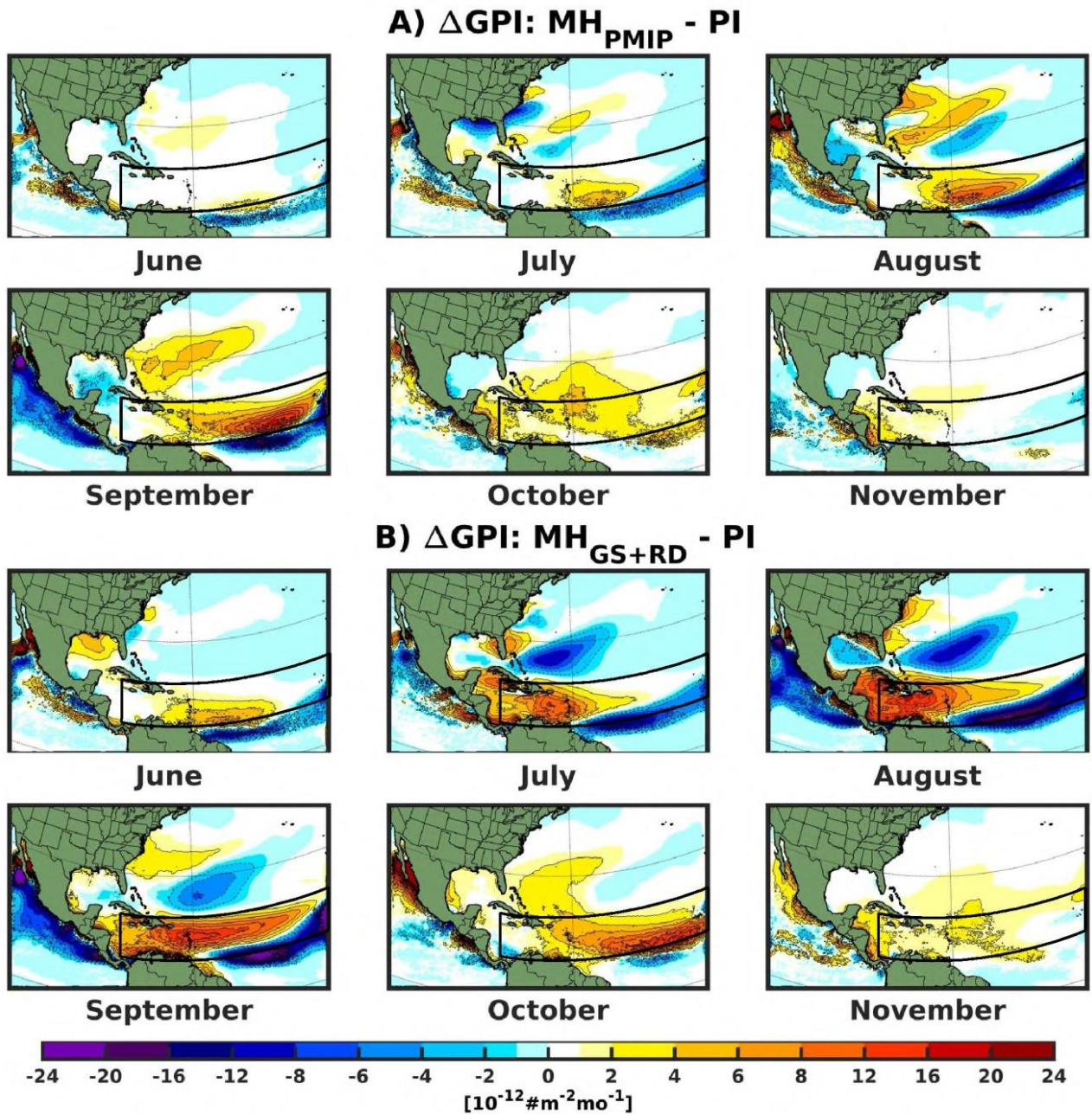
Figure 9: Changes in climatological monthly Genesis Potential Index (GPI) for A) MH$_{PMIP}$ and B) MH$_{GS+RD}$ relative to PI experiment. The black box shows the approximate present-day main development region (MDR). Only values that are significantly different at the 5% level using a local (grid-point) t test are shaded. The contour lines follow the colorbar scale (dashed, negative anomalies; solid, positive anomalies); the 0 line is omitted for clarity.
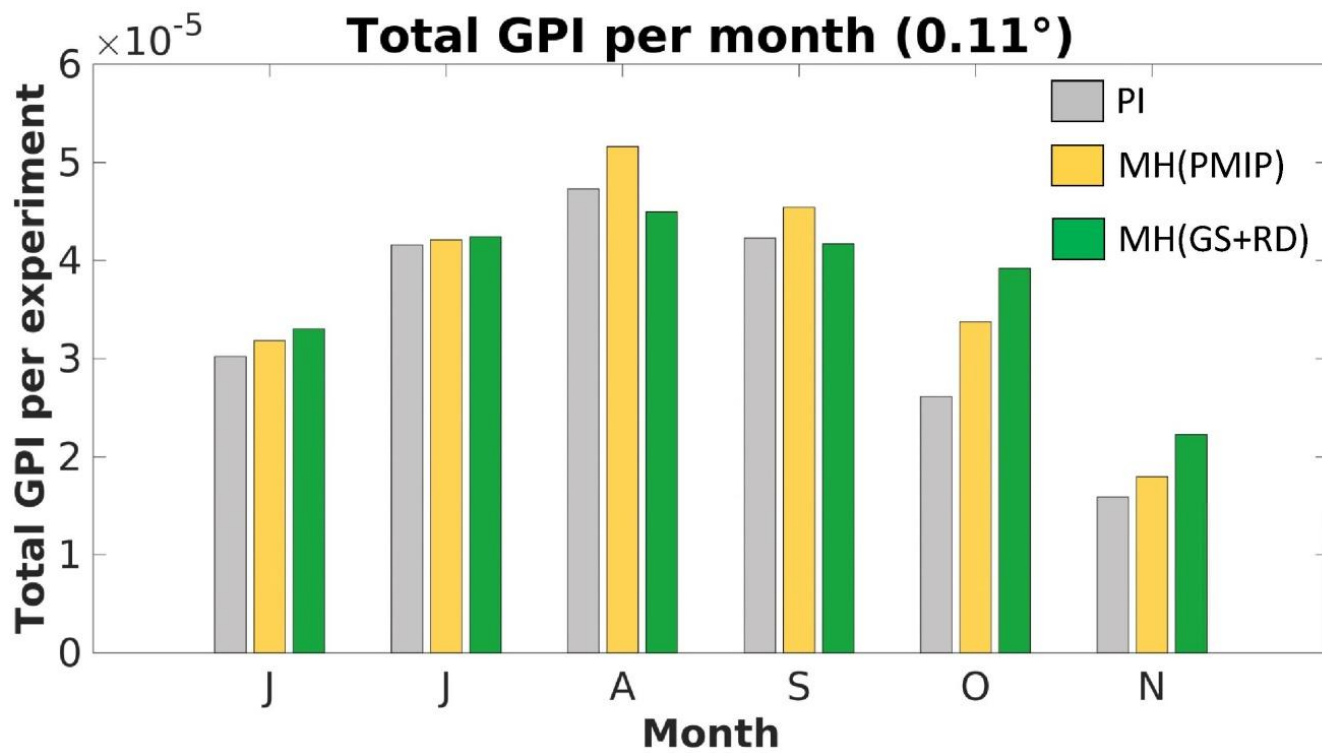
875

Figure 10: Seasonal variation (June to November) of the Genesis Potential Index (GPI) summed over the experimental domain for the three experiments.
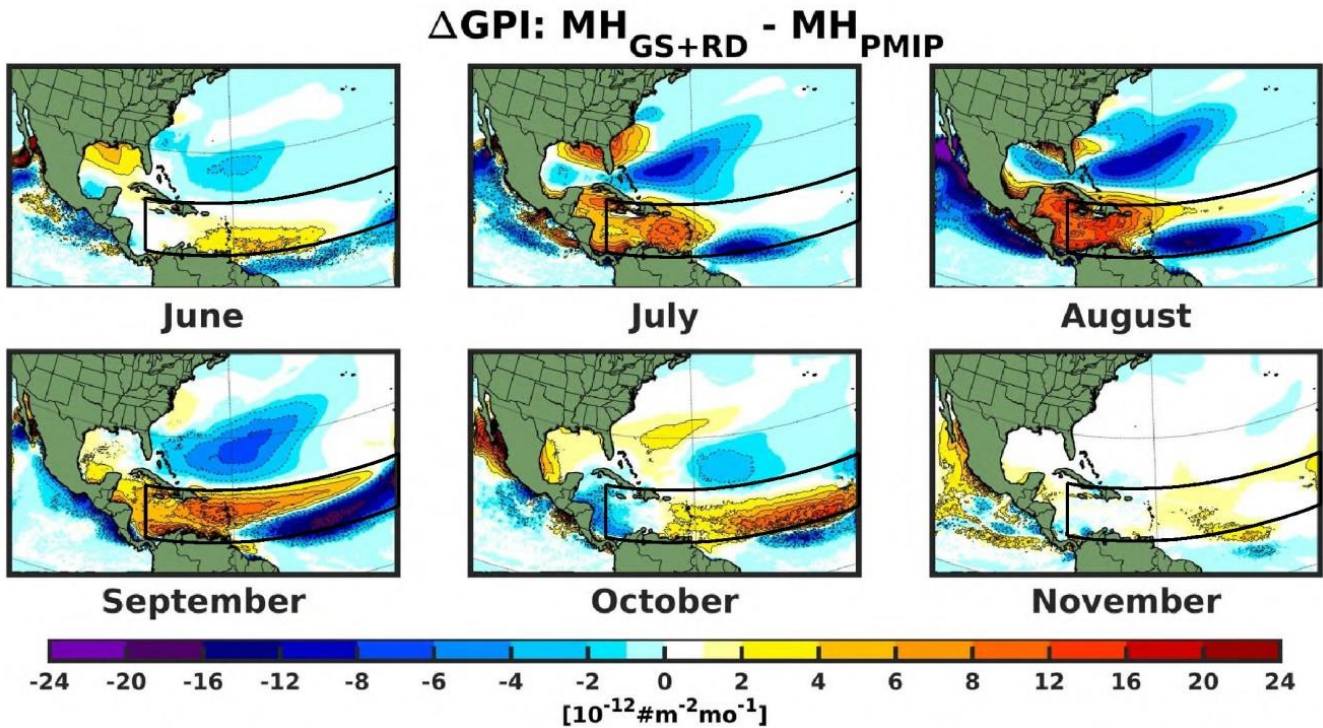
Figure 11: Changes in climatological monthly Genesis Potential Index (GPI) for MH$_{GS+RD}$ relative to MH$_{PMIP}$ experiment. The black box shows the approximate present-day main development region (MDR). Only values that are significantly different at the 5% level using a local (grid-point) *t* test are shaded. The contour lines follow the colorbar scale with different styles (dashed, negative anomalies; solid, positive anomalies); the 0 line is omitted for clarity.
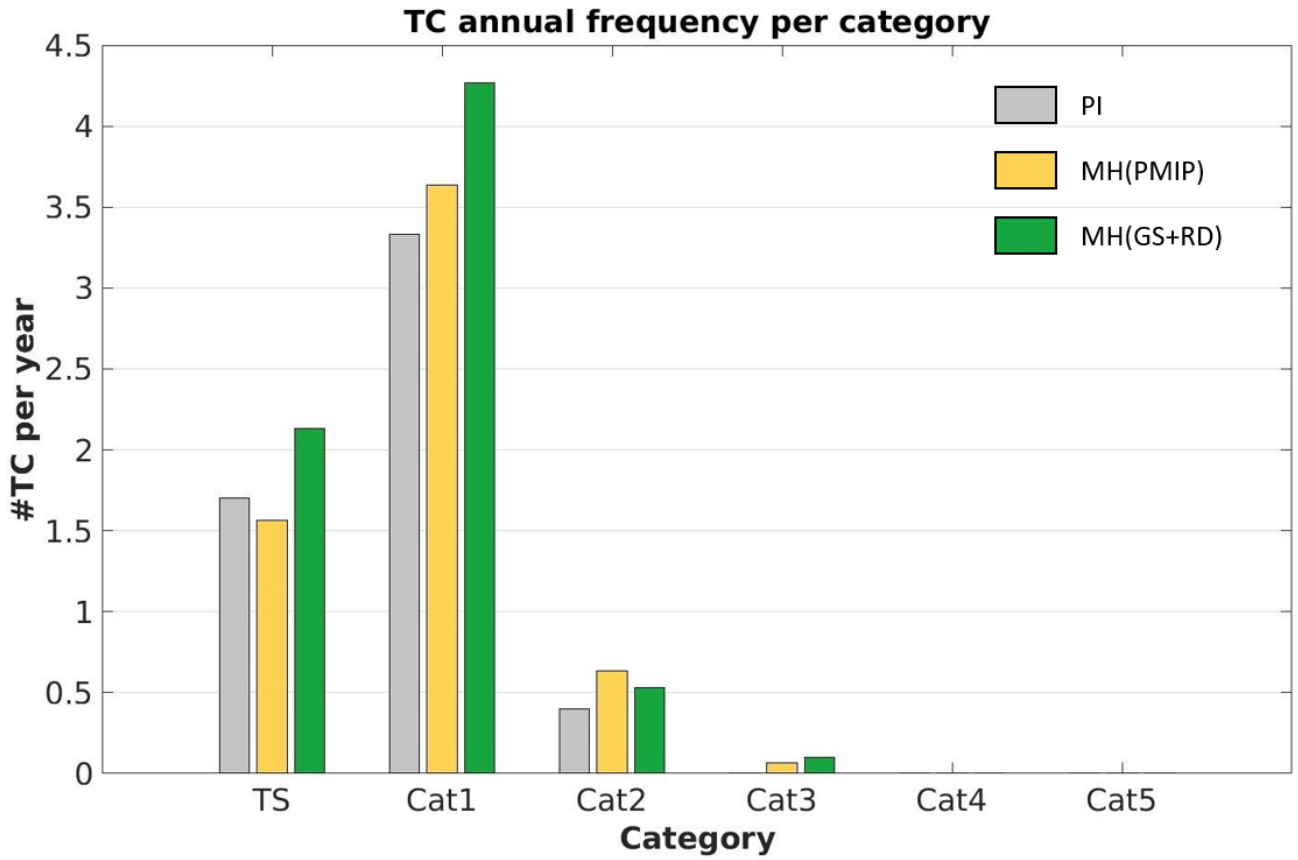
885

Figure 12: Climatological number of TC per year in various categories for the three experiment during the TC extended season (June to November; JJASON).
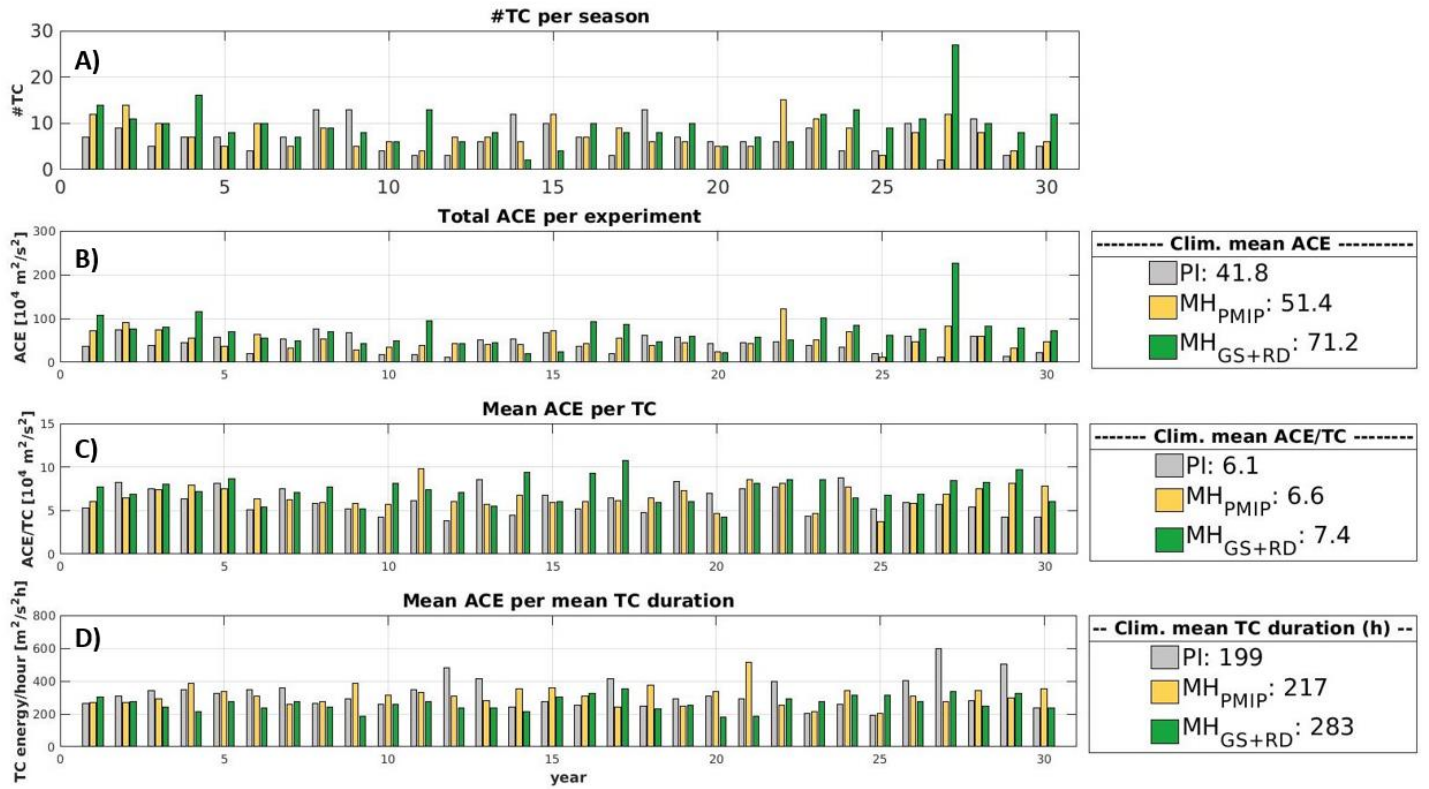
890 **Figure 13:** (A) Total number of cyclone per season for each experiment (30 years; Grey: PI, Yellow: MH$_{PMIP}$ and Green: MH$_{GS+RD}$). (B) Total Accumulated Cyclone Energy (ACE; $10^4 \, m^2s^{-2}$). (C) Mean ACE per cyclone per season ($10^4 \, m^2s^{-2}$). (D) Mean ACE per cyclone normalized by the mean tropical cyclone duration in every season ($10^4 \, m^2s^{-2}h^{-1}$). Legends present the climatological mean of each distribution.
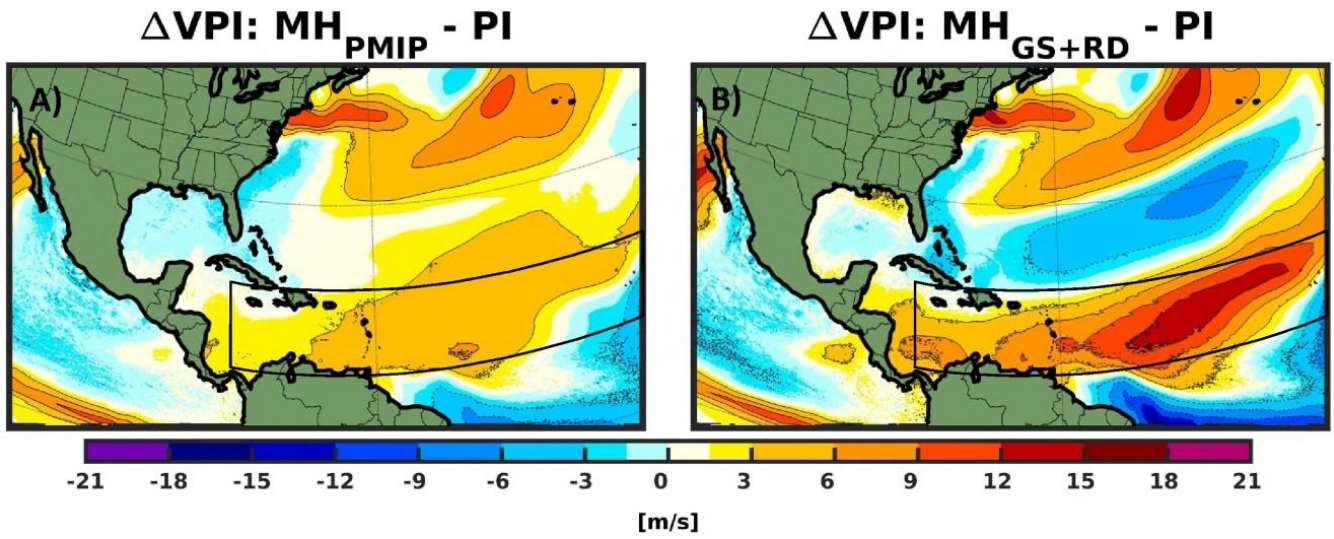
895

Figure 14: Changes in climatological seasonal VPI (June to November, JJASON) for (A) MH_PMIP and (B) MH_GS+RD experiments relative to PI. The black box shows the present-day main development region (MDR). Only values that are significantly different at the 5% level using a local (grid-point) t test are shaded. The contour lines follow the colorbar scale (dashed, negative anomalies; solid, positive anomalies); the 0 line is omitted for clarity.

900